

## RESEARCH ARTICLE

10.1002/2016JB013014

## Key Points:

- Two-dimensional surface wave focal spots are reconstructed from noise correlation functions
- Properties of the focal spot are controlled by local medium properties
- Wave speed, anisotropy, and apparent attenuation are estimated simultaneously

## Correspondence to:

G. Hillers,  
gregor.hillers@univ-grenoble-alpes.fr

## Citation:

Hillers, G., P. Roux, M. Campillo, and Y. Ben-Zion (2016), Focal spot imaging based on zero lag cross-correlation amplitude fields: Application to dense array data at the San Jacinto fault zone, *J. Geophys. Res. Solid Earth*, 121, 8048–8067, doi:10.1002/2016JB013014.

Received 22 MAR 2016

Accepted 10 OCT 2016

Accepted article online 12 OCT 2016

Published online 10 NOV 2016

## Focal spot imaging based on zero lag cross-correlation amplitude fields: Application to dense array data at the San Jacinto fault zone

G. Hillers<sup>1,2</sup>, P. Roux<sup>1,2</sup>, M. Campillo<sup>1,2</sup>, and Y. Ben-Zion<sup>3</sup>

<sup>1</sup>ISTerre, Université Grenoble Alpes, Grenoble, France, <sup>2</sup>CNRS, ISTerre, Grenoble, France, <sup>3</sup>Department of Earth Sciences, University of Southern California, Los Angeles, California, USA

**Abstract** We image the subsurface below a dense seismic array straddling the Clark branch of the San Jacinto fault zone in Southern California. The analysis is based on focal spots of surface waves associated with the zero lag amplitudes of noise cross-correlations computed between all stations of the dense array. Local medium properties are inferred from the spatially variable focal spot size and shape based on the first zero crossing of amplitude versus distance distributions. The method provides simultaneous estimates of wave speed, apparent attenuation, and anisotropy without solving a tomographic inverse problem. The obtained images of the frequency dependent seismic velocity distributions are consistent with independent estimates from a far-field Rayleigh wave tomography. We observe an anticorrelation between our apparent attenuation coefficient and seismic velocity, and a fault-parallel alignment of fast propagation directions with greater structural complexity to the southwest of the fault. The results imply a complex fault zone structure including a waveguide to the northeast of the fault that is continuous across the observed depth range and a low-velocity structure to the southwest associated with a shallow sedimentary basin.

### 1. Introduction

Seismic velocity structures are typically imaged using earthquake seismograms recorded in the far field. Tomographic techniques are also commonly applied to surface waves [Shapiro *et al.*, 2005; Sabra *et al.*, 2005] and body waves [Nakata *et al.*, 2015; Olivier *et al.*, 2015] reconstructed from ambient field correlations. Advanced techniques including the separation of waves and the tracing of irregular wavefronts and bent rays [Lin *et al.*, 2009; Mordret *et al.*, 2013; Boué *et al.*, 2014; Roux *et al.*, 2016] greatly extend the information gain from modern seismic arrays data compared to traditional methods. In contrast to these methods, the imaging technique used in this paper is based on data collected at subwavelength distances. In this sense it is a near field or local technique, although the analyzed noise cross-correlation wavefield does not contain evanescent near-field waves associated with point force excitation [Aki and Richards, 1980].

The technique is based on properties of the focal spot and has been used extensively in nondestructive testing, underwater acoustics, and medical ultrasound [Fink, 1999]. The term focal spot refers to the large-amplitude feature that emerges in time-reversal experiments around the origin. The equivalence of time reversal and cross-correlation [Derode *et al.*, 2001, 2003] is the basis for reconstructing the focal spot also from correlations of diffuse wavefields [Catheline *et al.*, 2008]. Using dense arrays data, the focal spot associated with any given station is obtained from the spatial distribution of noise correlation amplitudes at zero correlation time lag [Gallot *et al.*, 2011b; Hillers *et al.*, 2014].

Our analysis focuses on surface waves extracted from the ambient seismic noise field recorded by a dense 2-D seismic array (Figure 1) at the San Jacinto fault zone in Southern California [Ben-Zion *et al.*, 2015]. Evolving sensor technology is anticipated to lead to an increasing deployment of such very dense seismic arrays [Lin *et al.*, 2013; Mordret *et al.*, 2013]. To benefit from the obtained continuous recordings, it is essential to develop new imaging techniques and to adapt methods from other disciplines that handle data from high-resolution imaging devices.

Figure 2 illustrates the time-reversal process and the focal spot by showing spatial distributions of cross-correlation amplitudes at different lapse times  $\tau$ . The one-component sensors permit the reconstruction of vertical-vertical (ZZ) correlations only. In this example the reference station A is located at  $x_0 = 1.4\lambda$ ,

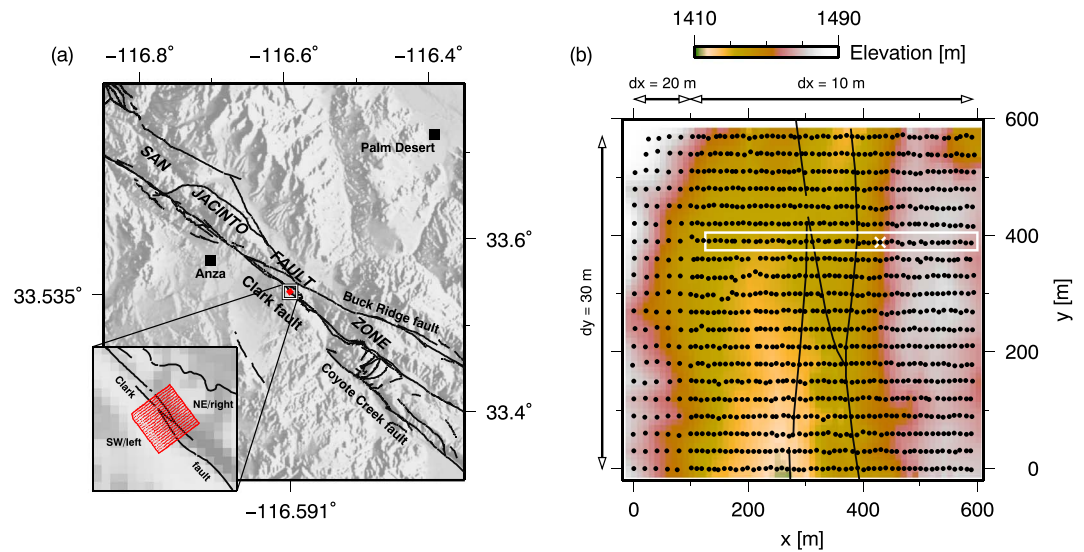


**Figure 1.** (a) Map of the San Jacinto fault zone study area. Black lines are mapped faults provided by the United States Geological Service. The area covered by the dense array is indicated by the red square. Southwest/northeast (SW/NE) and left/right of the fault are synonymous. (b) Actual locations of the sensors (black dots) on a Cartesian grid. The origin is indicated in Figure 1a by the longitude and latitude ticks. Black lines indicate the mapped fault traces. The range of variable interstation distances in the x direction is shown on top;  $dy = 30\text{ m} = \text{const.}$  Background colors indicate topography. The white cross and box indicate the reference station and the range used in Figure 3, respectively.

$y_0 = 1.4\lambda$ , where  $\lambda$  denotes the wavelength. At  $\tau = -1.1\text{ s}$  the field is characterized by background fluctuations. The converging wave refocuses at  $\tau = 0\text{ s}$  and then diverges at  $\tau > 0\text{ s}$  as if being emitted from location A. The circular amplitude pattern indicates isotropic propagation. In addition, linear wavefronts emerge parallel to the y axis and to the fault strike. These waves are manifestations of the heterogeneous fault zone structure.

The goal of this work is to demonstrate that the focal spot method is a useful complementary imaging tool in dense array seismology. We show that systematic estimates of the focal spot size and shape yield detailed images of wave speed and anisotropy of the crust below an array. This is important for understanding seismic ground motion and failure processes, crustal hydrology, subsurface reservoirs, designing filters for improved resolution at depth, and numerous other applications.

Reconstructing the focal spot directly from dense array data differs from previous applications of reversed wavefield propagation in geophysics. These include reflector imaging [Baysal et al., 1983], earthquake source imaging [McMechan, 1982; Rietbrock and Scherbaum, 1994; Larmat et al., 2006], and adjoint tomographic methods [Tromp et al., 2005]. The refocusing wavefields in these approaches are numerically simulated.

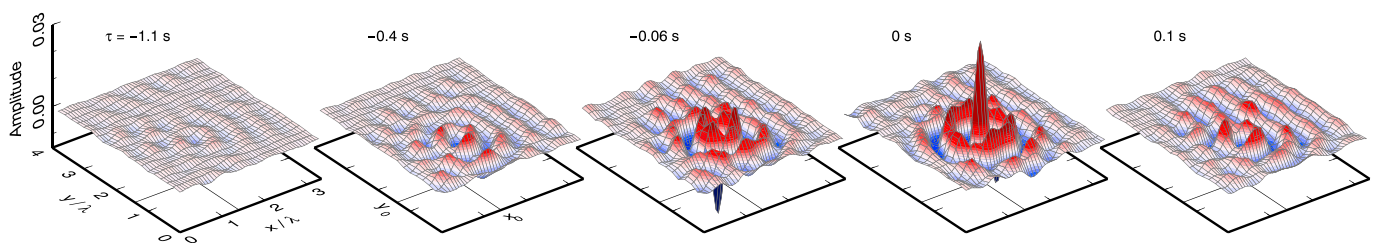


**Figure 2.** Snapshots of a converging ( $\tau < 0$ ), collapsing or refocusing ( $\tau = 0$ ), and diverging ( $\tau > 0$ ) surface wavefield illustrate the time-reversal process and the focal spot. The panels show wave number filtered (section 5.4) amplitude distributions of ZZ noise cross-correlation functions (8 Hz) obtained from the dense seismic array (Figure 1b) at different lapse times. We used data from  $x > 100\text{ m}$  where  $dx = 10\text{ m}$ . The viewing direction is north. The correlation reference station or virtual source is located at  $x_0 = 1.4, y_0 = 1.4$  on the wavelength-scaled axes. An interpolated autocorrelation value is used for the images. Waves aligned parallel to the y direction and to the fault strike indicate propagation that is influenced by the fault zone velocity structure. See Fink [2006], Catheline et al. [2008], and Gallot et al. [2011b] for similar sequences in acoustics, medical imaging, and seismics, respectively.

Focusing methods such as backprojection [Spudich and Oppenheimer, 1986; Ishii et al., 2005; Walker and Shearer, 2009] or beamforming [Capon, 1969; Rost and Thomas, 2002] do not model propagation from the source explicitly.

The relations between the cross-correlation of diffuse fields and the Green's function, and between correlation and time reversal, connect the focal spot method with the spatial autocorrelation method (SPAC) [Aki, 1957] (see section 2) and the microtremor H/V spectral analysis [Sánchez-Sesma et al., 2011]. However, we consider it more natural to discuss our time domain analysis of dense array data in the context of time reversal and refocusing (Figure 2); more evidence for this choice is given in section 7.2. The second-order time derivatives of displacement fields in the wave equation imply that the propagation of energy is time-reversal invariant. Together with source-receiver reciprocity, this means that for each diverging wave emitted from a source, there exists a related converging waveform that traces the same path in the opposite direction [Fink et al., 1989; Fink, 1997]. The backward propagating field eventually collapses or refocuses at the position of the original excitation (Figure 2).

Importantly, the emergent focal spot is of finite size, even for an ideal situation including a delta function source pulse and propagation in a lossless medium. This is because the time-reversed signals that are recorded in the far field do not contain evanescent near-field waves. The finiteness is thus a consequence of the local interaction of overlapping far-field wavefronts [Fink, 2006]. The spot size is controlled by the diffraction limit and therefore, in 3-D, proportional to one-half wavelength,  $\lambda/2$ . Focusing below the diffraction limit can be achieved by also replacing the source, not just the field, by its time-reversed analog called a sink [de Rosny and Fink, 2002].

Attenuation influences the performance of focusing techniques because it breaks the time-reversal invariance of the wave equation and is therefore important for propagation in a dissipating fault zone environment. However, the matched filter operation [Tanter et al., 2000, 2001] still maximizes the amplitude at the focus. That is, the focal spot emerges under a broad range of conditions because of the fundamental role of reciprocity, which explains the general robustness of the refocusing techniques.

The formal connection between time reversal and noise correlations [Derode et al., 2001, 2003] considers the medium response or Green's function  $h_{IJ}$  observed at location I associated with an emission at J. For a delta function excitation at a point S, the scalar wavefields recorded at A and B are the Green's functions  $h_{AS}(t)$  and  $h_{BS}(t)$ . The cross-correlation function C of the real-valued fields observed at the two stations is

$$C_{AB}(\tau) = \int h_{AS}(t + \tau)h_{BS}(t)dt \quad (1)$$

$$= h_{AS}(t) * h_{BS}(t), \quad (2)$$

where  $\tau$  is the time lag. Using the relation between correlation ( $*$ ) and convolution ( $\otimes$ ) [e.g., Smith, 1997]

$$h_{AS}(t) * h_{BS}(t) = h_{AS}(-t) \otimes h_{BS}(t), \quad (3)$$

the correlation function (equation (1)) can be expressed as

$$C_{AB}(\tau) = h_{AS}(-t) \otimes h_{BS}(t). \quad (4)$$

Employing spatial reciprocity  $h_{IJ}(t) = h_{JI}(t)$ , equation (4) changes to

$$C_{AB}(\tau) = h_{SA}(-t) \otimes h_{BS}(t). \quad (5)$$

Reversing the signal in a convolution algorithm yields the correlation (equation (3)). This is a mathematical similarity that appears in this context but does not reflect the time-reversal physics. Physical time-reversal enters the argument if we send a pulse from A that is sensed at S as  $h_{SA}(t)$ , then time reversed, and finally reemitted. By change of variables  $t \rightarrow t - T$ , with  $T$  being the time it takes for the pulse to travel from A to S, the field observed at B is given by equation (5), demonstrating that correlation and time reversal are equivalent.

This equivalence is illustrated in two end-member propagation regimes. In the multiple scattering regime one time-reversal mirror S is sufficient for isotropic refocusing. Correspondingly, the Green's function can be

retrieved from diffuse field correlations. On the other hand, continuously distributed stations S around A, B provide a perfect time-reversal mirror in a homogeneous medium. Azimuthal averaging is implemented by stacking the respective correlations to obtain the Green's function estimate.

In both regimes a finite-size focal spot emerges in the time reversed and in the correlation wavefields. Scatterers or noise sources away from the receiver pair make it impossible to reconstruct infinitely concentrated focusing from ambient field correlations. Hence, the notion that "a receiver acts as a source" accurately describes only the situation in the far field. The finiteness of the spot can be understood from the properties of the complete Green's function  $G$ . For the 2-D scalar case [Sánchez-Sesma and Campillo, 2006]

$$G(\omega) = -\frac{1}{4}\mu [Y_0(kr) + iJ_0(kr)], \quad (6)$$

where  $k = \omega/c$  is the wave number,  $\omega$  is the angular frequency,  $c$  is the phase velocity,  $r$  denotes distance,  $\mu$  is rigidity, and  $i$  is the imaginary unit. Considering that the correlation function  $C$  reconstructs the imaginary part of  $G$ , equation (6) shows that the diverging Neumann function  $Y_0$  does not enter the relation  $\partial C(r, \tau)/\partial \tau \propto G^+(r, \tau) - G^-(r, -\tau)$ . At  $r \rightarrow 0$ ,  $|\tau| \rightarrow 0$ , the correlation field is governed by the interaction of the finite Bessel functions  $J_0$ . The  $J_0(kr)$  proportionality describes not only the scalar case but also the ZZ component of the Rayleigh wave Green's tensor [Haney and Nakahara, 2014, equations (B5) and (B9)].

## 2. Focal Spot Parametrization and Implementation of the Method

The relationship between local medium properties and the focal spot size and shape forms the basis of our imaging method. Considering for example scalar wave propagation in fluids, time reversal leads to isotropic focal spots [Cassereau and Fink, 1992]. The amplitude distribution as well as the associated cross-spectral density are described by a sinc function [Cox, 1973]. In elastic solids the spherical symmetry of refocusing shear waves can be broken due to coupling between the source radiation pattern and the anisotropic properties of the vectorial elastic field [Catheline et al., 2008; Benech et al., 2009, 2013]. In section 5.2 we will demonstrate that azimuthally variable focal spot shapes also reflect the wave speed anisotropy of the propagation medium.

Wavefields in acoustics and elastography often contain only one mode of propagation. In contrast, wavefields in seismology typically contain more than one wave type. Our focus on surface waves suggests itself considering the dominance of Rayleigh waves in ZZ noise correlations obtained from vertical component data recorded at the surface of the Earth. A refocusing isotropic Rayleigh wavefront captured by the ZZ correlation field collapses in a focal spot with circular zero-amplitude contour [Gallot et al., 2011b]. Properties of ambient surface waves have long been studied in terms of the spatial autocorrelation, or SPAC [Aki, 1957]. For isotropic propagation the spatial correlation coefficient is equivalent to the complex coherency  $\gamma_{AB}(\omega)$  [Prieto et al., 2009; Liu and Ben-Zion, 2013] of seismic noise records. The coherency forms a Fourier pair with the noise cross-correlation function  $C_{AB}(\tau)$  (equation (1)) that is scaled by the power in the signals recorded at A and B. This connects SPAC to the time domain correlation and passive Green's function retrieval [Nakahara, 2006; Yokoi and Margaryan, 2008]. The correlation field at zero lag—the focal spot—constitutes the time domain equivalence of the spatial autocorrelation [e.g., Tsai, 2010]. Based on these interrelations, the inverse Fourier Transform at time zero of the band-limited coherency including attenuation [Prieto et al., 2009] yields to first order [Hillers et al., 2014]

$$A(r, \tau = 0) \approx \sigma J_0(kr)e^{-\alpha r}. \quad (7)$$

Expressions for the mixed components of the surface wave Green's tensor include combinations of higher-order Bessel functions [Haney et al., 2012]. This shape function describes the distance dependent amplitude distribution or focal spot shape at  $r < \lambda$  in the time domain. Importantly, the local wavelength is directly inferred from the spot size defined as the distance  $r^0$  of the first zero crossing of  $J_0(kr)$  [Abramowitz and Stegun, 1965; Ekström et al., 2009; Hillers et al., 2014]

$$r^0 = \frac{3}{8}\lambda. \quad (8)$$

This implies that  $r^0$  can be used to estimate the wave parameters  $k$ ,  $\lambda$ , and  $c$  at each frequency. The shape function (equation (7)) is chosen to obtain robust and easy  $r^0$  estimates from data at subwavelength distances. This approach uses more data and is therefore more robust compared to the linear approximation of the shape function in the vicinity of  $r^0$  [Haney et al., 2012].

The  $\sigma$  scaling factor and the  $e^{-\alpha r}$  term (equation (7)) are included to minimize the residual between our  $A(r, \tau = 0)$  data and the shape function for improved  $r^0$  estimates. We show that  $\sigma$  accounts for systematic scaling effects associated with data processing. The exponential term models the apparent attenuation of the focal spot data compared to a simple  $J_0$  function. We do not claim that  $\alpha$  is an accurate proxy for intrinsic attenuation or scattering attenuation usually parameterized by the quality factor  $Q$ . Hence, we refer to  $\alpha$  as *apparent attenuation coefficient*. It may also account for a potential distance dependence of  $\sigma$  within the limits of the decaying function.

Equations (7) and (8) constitute the backbone of our analysis that is implemented as follows. We first compute the cross-correlations between all array stations (Figure 1) in three frequency bands with constant bandwidth around 2, 4, and 8 Hz (1.5–3, 2.9–5.8, and 5.5–11 Hz). From this database we assemble the zero lag correlation amplitude fields  $A(x_0, y_0, x, y, \tau = 0)$ , where  $x_0, y_0$  refer to the position of the reference station or source and  $x, y$  indicate the locations of all receiver stations. In a key second step we implement a wave number filter to remove signatures of body waves and fault zone waves that interfere with the target surface waves. This yields a filtered surface wavefield  $\tilde{A}(x, y, \tau = 0)$  associated with a station at  $x_0, y_0$ . The imaging procedure consists of fitting  $\tilde{A}(r, \tau = 0)$  values with equation (7). This yields simultaneous estimates of  $\lambda, k$ , or  $c$  and the apparent attenuation coefficient  $\alpha$ . Application to data from variable azimuths resolves direction dependent wave speeds that is independent of a functional form of anisotropy. These observations characterize the medium around the location of the reference station  $x_0, y_0$ . The complete image is compiled by repeating the analysis for all positions. No spatial regularization or smoothing is applied.

The next three sections explain the data, the correlation processing, the wave number filter, and details of the imaging technique. In section 3 we provide additional information on the experiment. Section 4 describes the data and the construction of three sets of correlation functions that are used to investigate the effects of various processing choices on the analysis. Section 5 discusses in detail the preprocessing effects (section 5.1), wavefield and focal spot symmetry (section 5.2), general focal spot properties (section 5.3), wave number filtering (section 5.4), and the implementation of the imaging method (section 5.5).

### 3. The Array

We process data from a spatially dense 2-D array that was installed across the Clark Section of the San Jacinto fault zone (Figure 1a). The “large N” configuration consists of 1098 short period vertical component ZLand geophones that are arranged in 20 fault perpendicular line arrays packed into an area of  $600 \times 580 \text{ m}^2$ . The array recorded continuously for 30 days in May and June 2014 with a sampling rate of 500 Hz [Ben-Zion *et al.*, 2015]. Surveys of this scale were long reserved to the oil and gas industry only, but developments in sensor technology suggest that this type of deployment will become increasingly available to academic researchers. Our work contributes to extracting information on the subsurface structure from the resulting continuous and consequently massive data sets, by adopting an imaging technique that is usually applied to medical data from ultrasound transducers.

The nominal station spacing along the fault-parallel  $y$  direction is  $dy = 30 \text{ m}$ . Nominal interstation distances along the fault-perpendicular  $x$  direction vary between  $dx = 20 \text{ m}$  and  $dx = 10 \text{ m}$  at distances smaller and larger than  $x = 100 \text{ m}$ , respectively (Figure 1b). The topography varies between 1410 m (at  $x = 220 \text{ m}, y = 0 \text{ m}$ ) and 1490 m (at  $x = 0 \text{ m}, y = 580 \text{ m}$ ). The origin is defined to be the position of the station in the lower left corner of the grid. The local strike of the fault is in a northwest-southeast direction ( $\approx \text{N}143^\circ\text{E}$ ).

### 4. Data and Correlations

We make three correlation databases or sets from the continuous noise data that are downsampled to 100 Hz. Sets I and II are used for testing, to study different features of the spatial amplitude distributions, and to investigate data processing and scaling effects. The results are discussed in sections 5.1 and 5.2. Set III is used for the imaging from section 5.3 onward. The three sets differ by the number of stations, frequency range, the time window of the used data, and the applied data processing (Table 1).

The wavefield recorded by the array is not stationary, which is evident from the many spikes and transients of variable amplitude and duration in the raw data likely reflecting ongoing failures in the crust below the array [Ben-Zion *et al.*, 2015]. Before correlation, it is therefore necessary to make the wavefield properties more

**Table 1.** Summary of the Processing Sequences<sup>a</sup>

Set	Configuration	Window	Segment	Frequency	Processing	<i>k</i> Filter
Ia	line array (line 14, $y = 390$ m)	15 days	30 min	2 Hz	whiten, 1 bit clipping	no
Ib		15 days	30 min	2 Hz	whiten, SD clipping	
IIa	$\left\{ \begin{array}{l} dx = dy = 30 \text{ m grid} \\ +58 \text{ stations along edges} \end{array} \right\}$	15 days	60 min	2 Hz	correlations as in Ia	no
IIb		coda of IIa correlations		2 Hz	$C^3$ functions	
III	all stations	30 days	10 min	2, 4, and 8 Hz	whiten, 1 bit clipping	yes

<sup>a</sup>See section 4 for explanations. Segment refers to the division of the windowed data for preprocessing and correlation. The frequency band is defined by the whitening filter; *k* filter refers to filtering in the wave number domain (section 5.4). SD abbreviates standard deviation.

compatible with that of an isotropic, diffuse field approaching equipartition [Hennino *et al.*, 2001; Sánchez-Sesma and Campillo, 2006]. This is usually done by the application of normalization techniques in the time domain and in the frequency domain, which greatly affects, however, correlation amplitudes [Cupillard and Capdeville, 2010; Prieto *et al.*, 2011; Tsai, 2011]. The correlation set I is used to study the effects of two different time domain clipping techniques on the focal spot (section 5.1) and to discuss the  $\sigma$ -scaling (equation (7)). We preprocess data from 15 days using 30 min segments. After application of whitening in the low-frequency band around 2 Hz, the data in each window are 1 bit clipped (set Ia) or standard deviation clipped (Ib). The latter refers to clipping the amplitudes in each 30 min window at—in this case—3.5 times the standard deviation of the amplitude distribution in that window. We consider stacked correlations between the station located at  $x_0 = 430$  m,  $y_0 = 390$  m and all other stations in that line up to  $r = 300$  m.

We make two data sets to study the effects of directionality on the spatiotemporal correlation amplitude symmetry (section 5.2). Set IIa is used to demonstrate the effects of nonisotropic propagation of the incident wavefield. We use again data from a 15 days window, cut the seismograms into 1 h segments, apply whitening in the 2 Hz band and the 1 bit normalization. We use stations from a reduced grid that extends from  $x = 100$  m to  $x = 580$  m and from  $y = 60$  m to  $y = 510$  m considering a homogeneous station spacing of  $dx = dy = 30$  m. For set IIb we compute  $C^3$  functions [Stehly *et al.*, 2008] between the reference station at  $x_0 = 350$  m,  $y_0 = 270$  m and all other stations on the grid.  $C^3$  functions are obtained by recorrelating the coda of noise correlation functions. This typically enhances the signature of the medium and reduces directional propagation effects of the original noise wavefield. The iteration of the correlation procedure also allows the tuning of incident wavefield directions by choosing the distribution of stations acting as virtual sources. We use 58 stations along all four edges as virtual sources and recorrelate noise correlation coda between  $10 \text{ s} < |\tau| < 100 \text{ s}$ .

The final set III consists of the full database of all-to-all correlation functions using all data. Records are cut into 10 min segments, whitened in the three frequency bands, 1 bit clipped, correlated, and stacked after application of some quality control. The short segments together with the 1 bit clipping were found to yield the best signal-to-noise ratio of the resulting waveforms.

## 5. Analysis

We illustrate the effects of different data processing chains on properties of the correlation wavefields and discuss implications for the wavelength estimates from the size and shape of the emerging focal spots. We show that strong body wave components inhibit a clean reconstruction of the refocusing surface wave, present a strategy that removes these interfering components, and discuss the measurements of wave propagation properties from the clean focal spots.

### 5.1. Amplitude Effects

Figure 3a shows the distance dependent amplitude values (dots) of the cross-correlation function sets Ia and Ib. These line array data are not wave number filtered (section 5.4); the data do not represent clean surface wave focal spots but are still adequate to illustrate the  $\sigma$  scaling. As expected, the autocorrelation values at the origin equal unity in all cases (not shown). The order-of-magnitude smaller values at small distances reflect the high level of incoherent noise. The amplitudes between the tested 1 bit and standard deviation clipping results vary by 50%. This large difference highlights the challenge to accurately estimate medium characteristics from correlation amplitude. Results of fitting  $A(r, \tau = 0)$  data with equation (7) are shown in Figure 3a by

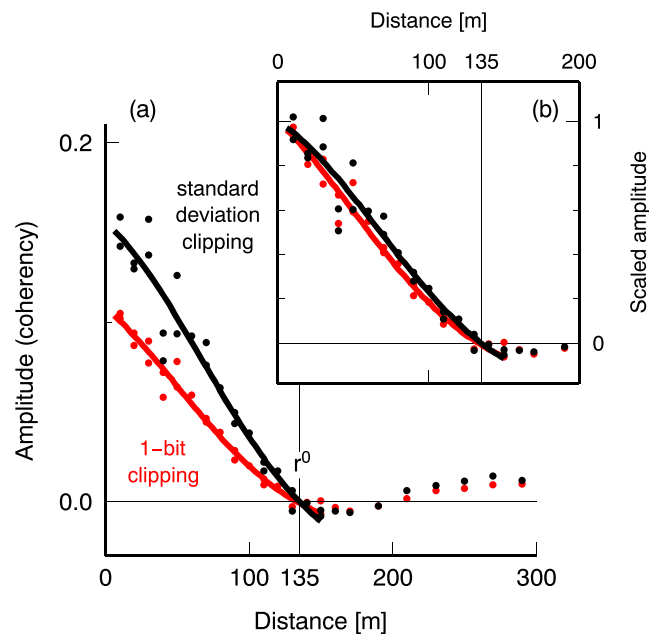


**Figure 3.** Cross-correlation amplitude distributions  $A(r, \tau = 0)$  associated with correlation set I (2 Hz, red: set Ia, black: set Ib) using the reference station located at  $x_0 = 430$  m,  $y_0 = 390$  m and data along that line (white domain in Figure 1b). (a) Amplitudes associated with two different preprocessing procedures. (b) The data in Figure 3a scaled by the  $\sigma$  factor in equation (7).

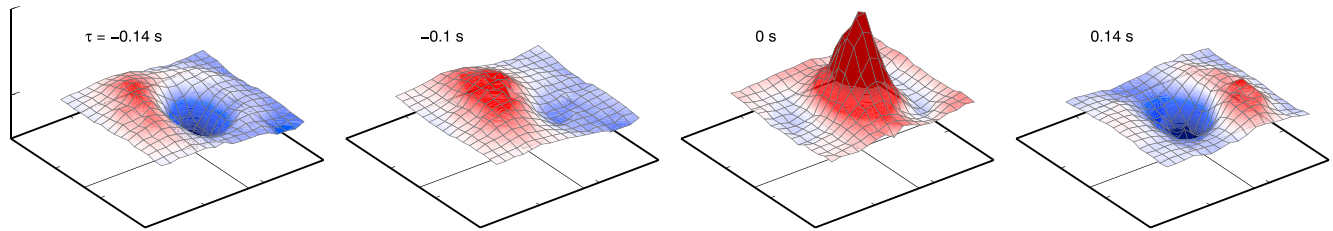
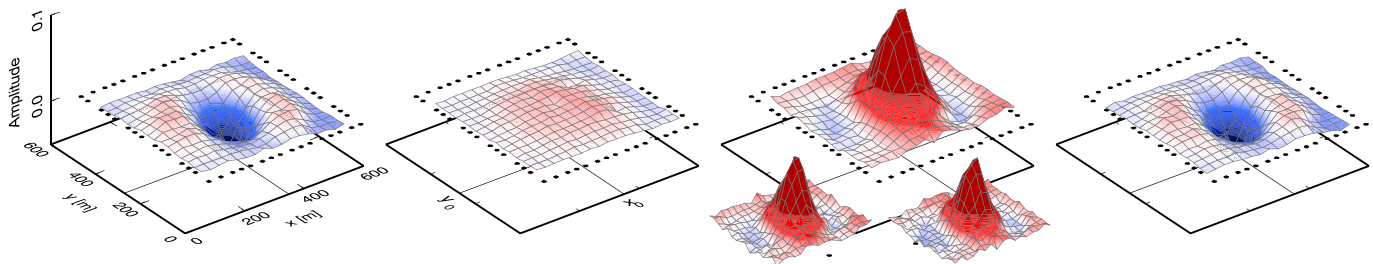
the solid lines. The distance range is limited to the first minimum of  $A(r, \tau = 0)$ . We return to this choice and discuss the data fitting in more detail in section 5.5. Importantly, if amplitudes are scaled by the obtained  $\sigma$  values (Figure 3b), the two populations corresponding to 1 bit clipping (Ia, red data) and standard deviation clipping (Ib, black data) coincide and the same zero crossing distance  $r^0$  of about 135 m is obtained from both solutions. This distance can already be inferred from the unscaled data in Figure 3a. The remaining differences between the scaled data sets, and the incompatibility with the  $J_0$  model at  $r > r^0$ , are attributed to interfering wavefield components. In conclusion, the scaling factor  $\sigma$  is essential to account for systematic differences in the amplitude level; a potential dependence on  $r$  is not explicitly considered. Estimates of the root-controlling wave number  $k$  and the associated wave parameters are insensitive to the amplitude-affecting preprocessing.

### 5.2. Wavefield Symmetry and Iteration of the Correlation Procedure

To study effects of anisotropic propagation on the focal spot shape, we first consider 2-D cross-correlation amplitude distributions associated with set IIa. Here and also for the results obtained with the complete set III, the shape of the focal spot—the contour of  $A(x, y, \tau = 0) = 0$ —is not circular everywhere but exhibits a spatially variable degree of anisotropy. The contour shape can be better described by an ellipse with variable aspect ratio and azimuthal inclination. What causes these anisotropic focal spot shapes? The effect of a direction dependent Rayleigh criterion associated with the source radiation pattern [Catheline et al., 2008; Benech et al., 2013] can be ruled out here. Isotropic radiation associated with vertical excitation in the ZZ configuration yields circular spots [Gallot et al., 2011b]. The major axis of the obtained low-frequency focal spots is generally oriented parallel to the strike of the San Jacinto fault (section 6). This feature can be governed by anisotropic local medium properties. Alternatively, the anisotropy is spurious and caused by the propagation directions of the incident wavefield from which the correlation functions are constructed. This is plausible for the lower frequencies inasmuch the fault strike is parallel to the region of the noise excitation along the Pacific coastline west of the site [Schulte-Pelkum et al., 2004; Gerstoft and Tanimoto, 2007; Hillers et al., 2013]; noise up to 10 Hz is also excited in the same fault-normal direction [Ben-Zion et al., 2015].

Spatial amplitude patterns of the noise correlation set IIa at negative and positive lag times indeed show that energy propagates predominantly in a southwest-northeast (SW-NE) direction perpendicular to the fault (Figure 4a). The change from the correlation distributions  $A(x, y, \tau)$  at nonzero lag times to the  $C^3$  results (set IIb; Figure 4b) demonstrates that the homogeneous virtual source distribution yields more isotropic patterns. The signatures of the excitation to the west are significantly reduced, which illustrates the denoising effect of

(a) Noise correlation amplitudes


 (b)  $C^3$  function amplitudes


(c) Zero-amplitude contours

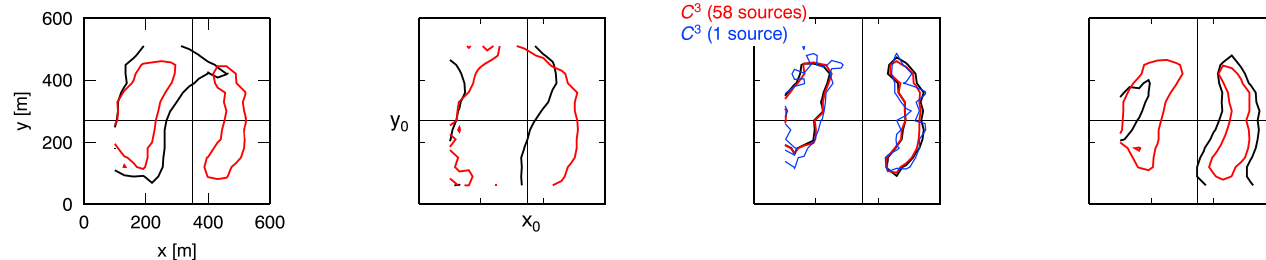


**Figure 4.** (a) Cross-correlation amplitude distributions  $A(x_0, y_0, x, y, \tau)$  at different lapse times from correlation set IIa (2 Hz) illustrate the incident, directional propagation. The fields are not wave number filtered. (b) The associated  $C^3$  function (set IIb) amplitude distributions are characterized by azimuthally symmetric propagation directions. Black dots indicate the locations of the 58 virtual source stations. Insets at  $\tau = 0$  s show the spots obtained with one virtual source. (c) Zero-amplitude contours of the distributions in Figures 4a (black) and 4b (red). The blue contour at zero time corresponds to the focal spot associated with one virtual source located at the SW edge of the grid. The reference station is not part of the receiver station grid for which  $dx = dy = 30$  m. The viewing direction is north.

the recorrelation procedure [Hillers *et al.*, 2012, 2015]. Therefore, the persistent systematic amplitude variation between the fault-normal and fault-parallel directions imply anisotropic medium properties.

In contrast to these  $|\tau| > 0$  s results, the identical contours in Figure 4c highlight the shape invariance of the focal spots obtained from the two data sets. This insensitivity to a predominant energy flux suggests that the reconstruction of focal spots is robust. Remarkably, we obtain the same symmetric focal spot patterns by using 58 sources or just one virtual source (insets in Figure 4b at time zero). This is additional strong evidence that the spot anisotropy is a manifestation of direction-dependent wave speeds in the fault zone environment.

### 5.3. Properties of Zero Lag Amplitude Distributions: Focal Spots

We proceed with the analysis of the full correlation database, set III. Figure 5a (top row) shows example focal spots at different frequencies for different reference stations. We note that the different preprocessing parameters make the set III wavefields more symmetric compared to the fields obtained from set IIa. This, too, implies that the spot anisotropy is not a result of noise directionality. It highlights the importance of data processing choices in fault zone environments [Hillers and Campillo, 2016] with its many different wave types including body waves, head waves, and trapped waves. General properties of the obtained amplitude distributions are frequency dependent, e.g., lowest coherency values are found at low frequencies due to the sensor characteristics [Roux *et al.*, 2016].

Two features of the  $A(x_0, y_0, x, y, \tau = 0)$  fields interfere with an accurate estimate of  $r^0$  or  $k$ . First, small-scale cell-to-cell fluctuations affect mainly estimates at short wavelengths where few data points can be used in

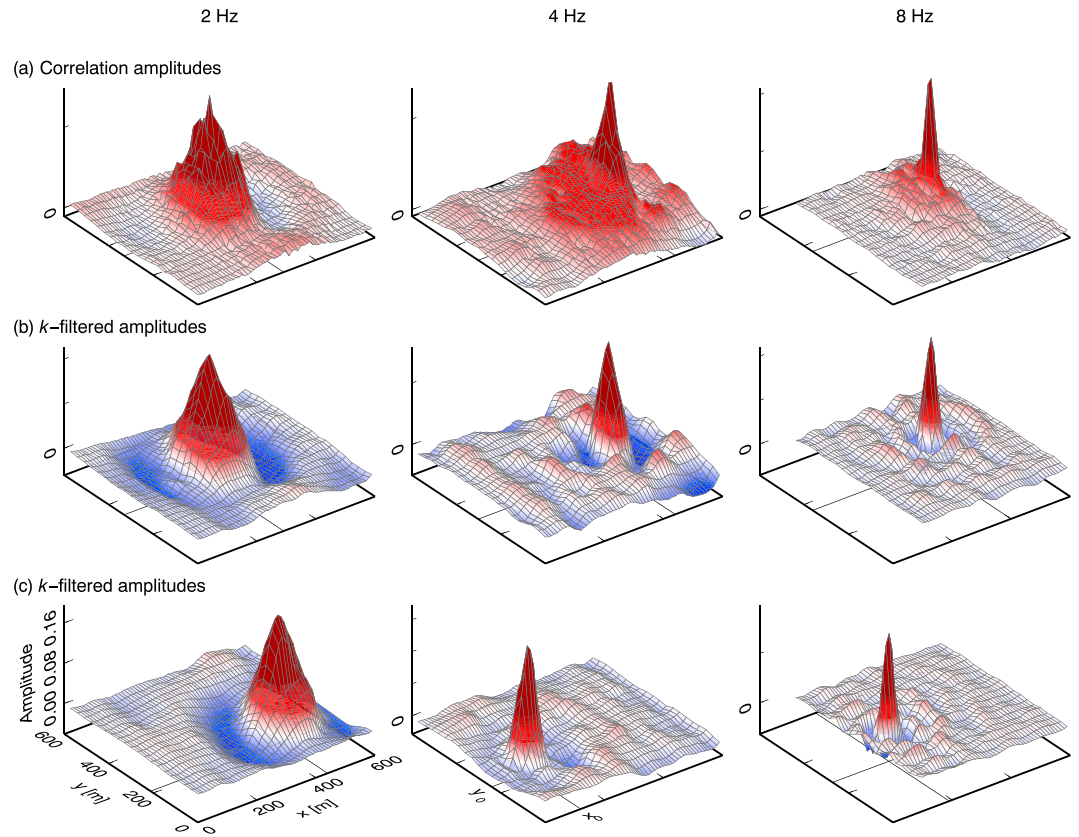


**Figure 5.** Focal spots, that is, zero lag correlation amplitude distributions for the three frequencies. (a) Original  $A(x, y, \tau = 0)$  distributions associated with three different reference locations  $x_0, y_0$ . (b) Corresponding  $\bar{A}(x, y, 0)$  data after wave number filtering. (c)  $\bar{A}(x, y, 0)$  fields for another set of reference stations. Autocorrelation values are interpolated. At 2 Hz and 4 Hz values are interpolated to a  $dx = 10$  m interval at  $x < 100$  m for the purpose of visualization. At 8 Hz the analysis is limited to  $x > 100$  m where  $dx = 10$  m. The z axes are adapted to the minimum and maximum value in each case. The z tick interval is uniform 0.08. The viewing direction is north.

fitting the shape function. Second, the base of the focal spot is immersed in positive amplitude values that extend over a region that can be larger than  $\lambda$ . This effect is strongest at intermediate and high frequencies (Figure 5a; 4 Hz and 8 Hz). It inhibits  $r^0$  estimates in the first place because no negative amplitudes mean no zero crossing. The region of positive coherency at zero lag time indicates waves that arrive with a very high apparent velocity, that is, from below. These are signatures of body waves from numerous events below the array or fault zone waves that interact with (or are trapped within) the low-velocity waveguides in the fault zone environment.

#### 5.4. Wave Number Filtering

To mitigate small-scale fluctuations and remove contributions from waves with high apparent velocity for improved  $r^0$  estimates, we filter the  $A(x, y, \tau = 0)$  distributions in the wave number domain (Figure 6a). We remove the mean value from  $A(x, y, \tau = 0)$  and apply a 2-D discrete Fourier transform (DFT). This yields  $F[A](k_x, k_y)$  distributions, where  $k_x$  and  $k_y$  denote wave numbers associated with the x and y direction, respectively (the description refers to absolute  $k$  values). We make a wave number bandpass mask  $M(k_x, k_y)$  that has Gauss tapers between zero and unity around a small- $k$  limit  $k_s$  and between unity and zero around a large- $k$  limit  $k_l$ . The modulus of the field  $F[A](k_x, k_y)$  (Figure 6b) is then multiplied by  $M(k_x, k_y)$  (Figure 6c). Application of an inverse DFT using the original phase information yields cleaned focal spots  $\bar{A}(x, y, \tau = 0)$  (Figure 6d) from which the first zero crossing distance associated with a surface wave number can be estimated.

Choices of  $k_l$  and  $k_s$  reflect length scale ( $k_l \equiv 2\pi/\lambda$ ) and slowness ( $k_s \equiv f/c$ ) limits, respectively. To damp fluctuations on scales of the largest minimum interstation distance  $dy = 30$  m (Figure 5), energy is suppressed above the frequency independent low-pass wave number  $k_l = 100 \text{ km}^{-1}$ . This value is just slightly smaller than the Nyquist wave number  $k_y = 104 \text{ km}^{-1}$  associated with the nominally constant  $dy = 30$  m spacing.

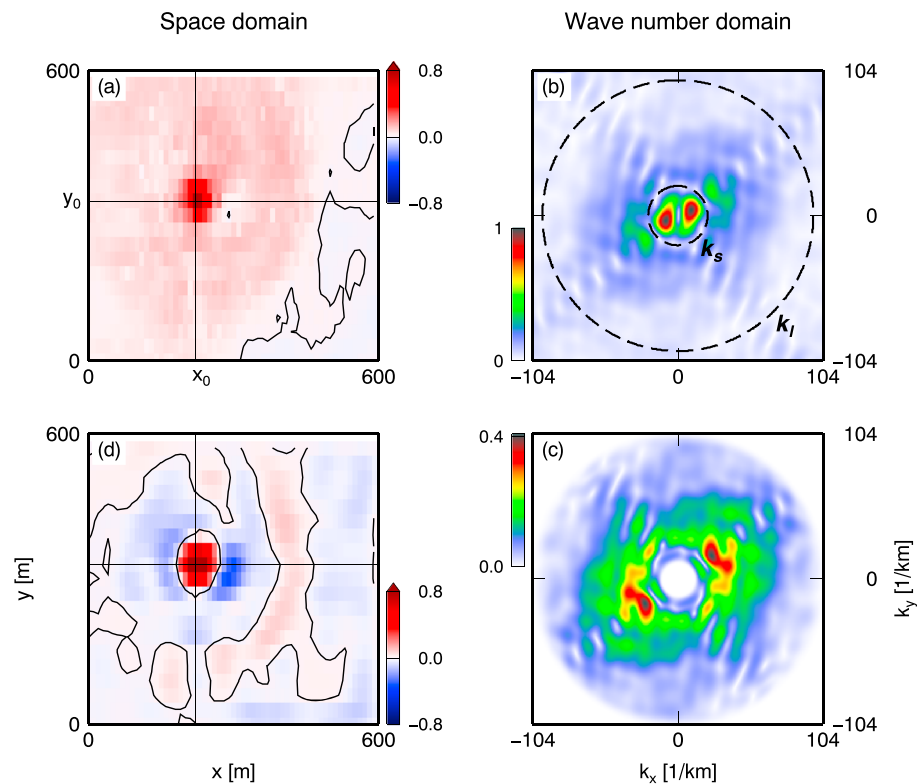


**Figure 6.** Illustration of the wave number filtering. (a) Scaled cross-correlation amplitude distributions  $A(x, y, \tau = 0)$  (4 Hz) associated with a reference station at  $x_0 = 220$  m,  $y_0 = 330$  m. (b) Amplitudes in the wave number domain, that is, the modulus of  $F[A](k_x, k_y)$ . The dashed lines indicate the corner wave numbers  $k_s$  and  $k_f$  of the bandpass filter. (c) The filtered amplitude distribution in the wave number domain, that is, the modulus of  $F[A](k_x, k_y)$  weighted by the bandpass mask. Amplitudes are scaled by the maximum in Figure 6b. (d) The scaled amplitude distribution in the space domain  $\tilde{A}(x, y, 0)$  after inverse Fourier Transform. An interpolated value instead of unit autocorrelation is used in Figure 6a and in the following calculations. In Figures 6a and 6d values are interpolated to a  $dx = 10$  m interval at  $x < 100$  m for the purpose of visualization.

Reducing  $k_f$  below  $\sim 80 \text{ km}^{-1}$  impairs the resolution provided by the dense deployment. The increased damping mostly affects the focal spot reconstruction and the wavelength estimates at higher frequencies. Energy associated with apparent propagation speeds exceeding  $c_s = 1 \text{ km/s}$  is removed at wave numbers that are smaller than the frequency-dependent high-pass limit  $k_s = f/c_s$ . The choice of  $c_s$  follows the observation that Rayleigh group wave speeds in the considered frequency range do not exceed  $800 \text{ m/s}$  [Roux et al., 2016]. The lower frequency limit of each band is used to define  $k_s$ . Varying  $c_s$  between  $0.8 \text{ km/s}$  and  $2 \text{ km/s}$  does not change our results.

The energy distribution in the  $k$  domain obtained from the zero lag amplitude field is anisotropic (Figure 6c). The similarity with results from far field surface wave data [Roux et al., 2016] indicates that the azimuthal distribution is possibly influenced by the fault-normal energy flux. However, as shown in the symmetry analysis (section 5.2), the obtained anisotropic focal spot (Figure 6d) is related to medium properties and insensitive to the directional propagation encountered here. Filtering can be further optimized to mitigate these directionality effects [Gallot et al., 2011b]. We iterate that the removal of body wave and fault zone wave energy at small wave numbers is essential for the application of the surface wave focal spot parameterization (section 2 and equation (7)).

### 5.5. Estimating Medium Characteristics From Amplitude Distributions

We only fit  $\tilde{A}(r, \tau = 0)$  data (Figure 7) at short distances  $r < \lambda$  for several reasons. The distributions at  $r \geq \lambda$ , that is, at distances of the second zero crossing and beyond, is generally heterogeneous and uncorrelated with the shape or contour of the first root, which is controlled by the strong velocity variations. This effect is strongest at intermediate and high frequencies (4 Hz and 8 Hz; Figure 6d) and depends on the location of the reference station. We limit the range to distances that are not affected by these irregularities to improve the fit. This

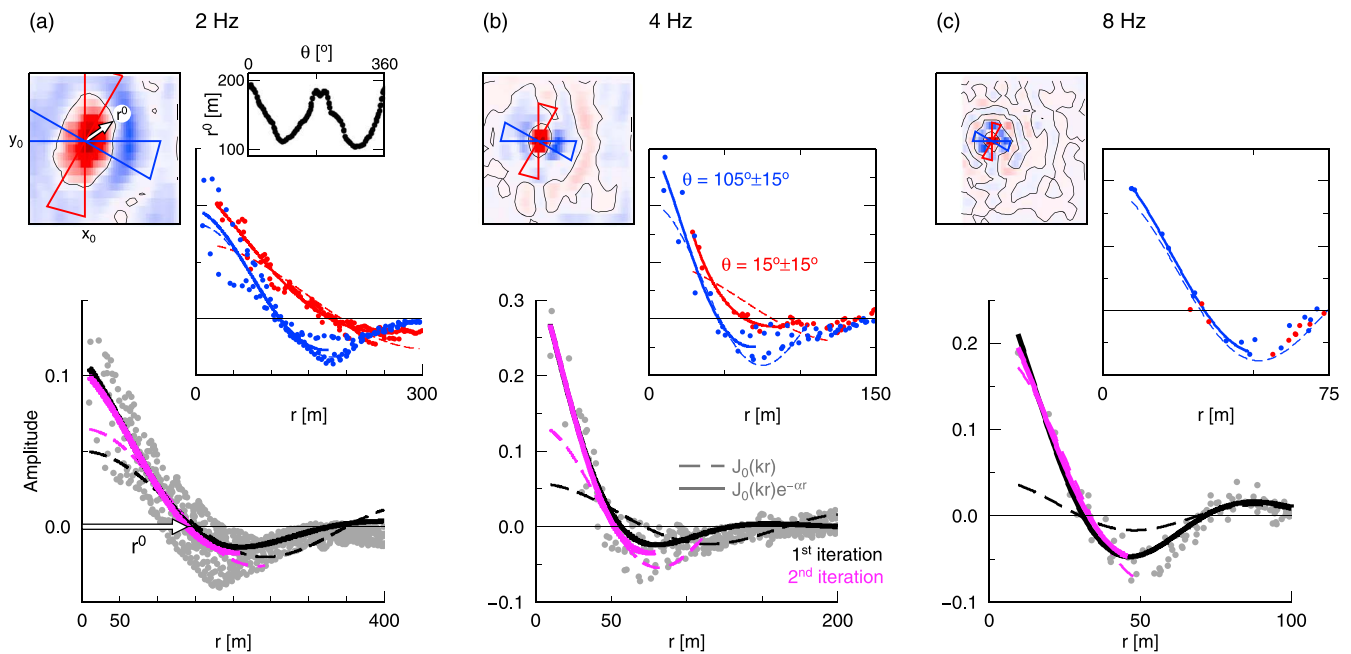


**Figure 7.** (a–c) Estimating the zero crossing distance  $r^0$  from wave number filtered correlation amplitude distributions associated with a reference station at  $x_0 = 220$  m,  $y_0 = 330$  m. In each panel, the top figure shows the amplitude distribution. Black contours trace the zero level. The domain and color range is the same as in Figure 6d. The length of the azimuthal delimiters corresponds to the  $r$  axis in the associated center figures. The analysis at 8 Hz is limited to the range where  $dx = 10$  m. The center figure shows the data and shape function (equation (7)) fits at  $180^\circ$  periodic  $\theta = 15^\circ$  and  $\theta = 105^\circ$ . Figures 7a (bottom) to 7c (bottom) show the azimuthally independent fit to all data. The  $r^0 = f(\theta)$  inset in Figure 7a shows azimuthally dependent zero crossing estimates from the map view figure to the left. It highlights the  $180^\circ$  periodicity. Data in Figure 7c indicate that the dependence on azimuth cannot be resolved at this wavelength and station spacing and that the  $c$  estimates are dominated by variations along  $\theta = 90^\circ$  where  $dx$  is small. The center and bottom figures in Figures 7a to 7c share the range and ticks on the  $y$  axis.

highlights distances associated with the first root instead of estimating  $k$  from far-field data at large  $r$  [Prieto et al., 2009; Ekström et al., 2009]. The adopted near field approach is much less sensitive to wave propagation that is nonisotropic at distances greater one wavelength. Choosing  $r < \lambda$  also allows the application of the analysis to wavelengths on the order of the array size, which can not be achieved using far-field methods.

We estimate  $r^0$  and  $\alpha$  using a two-step process. We first fit the complete  $\bar{A}(r, \tau = 0)$  population with the Bessel function model (equation (7); the autocorrelation value is not included) using MATLAB's implementation of a nonlinear least squares data fitting algorithm. The removal of energy through the filtering process affects the original amplitude estimate, which further supports the use of the scaling factor  $\sigma$  in equation (7). This process is then repeated by limiting the fit distance to the position of the first minimum of the initial estimate. The first minimum of the  $J_0(kr)$  function is at a distance of about  $0.6\lambda$ . This yields  $r^0$ ,  $k$ , and  $\alpha$  estimates, confidence intervals, and a standard or root-mean-squared (RMS) error estimate  $\epsilon$  that quantifies the residual between data and the best fitting shape function.

As mentioned in section 2,  $\sigma$  and the  $e^{-\alpha r}$  term are included in equation (7) for improved data fitting and hence  $r^0$  estimates. Setting  $\alpha = 0$  yields systematically poorer fits, but the obtained velocity images contain nevertheless the same main features as the results discussed below. This consistency implies that the exponential term is not fundamental to obtain reasonable wave speed estimates (the position of the zero crossing controls the solution). However, the agreement between the attenuated shape function and the data is much better compared to just  $\sigma J_0(kr)$  (Figure 7). Interestingly, the relation between the obtained  $\alpha$  and wave speed patterns is compatible with many previous observations on the relation of velocity and the quality factor  $Q$ . It implies the possibility that the apparent attenuation parameter  $\alpha$  captures physical attenuation to some degree, and we therefore include the distributions in the discussion, where we focus on the spatial variability instead of absolute values.

We investigate the azimuthal variability of the spot shape (Figure 7). The two-step fitting process is applied to directional  $\bar{A}(r, \tau = 0)$  data by taking amplitude values in an angle  $\pm d\theta/2$  around a central direction  $\theta$  that is  $180^\circ$  periodic. The periodicity considers the generally observed  $2\theta$  variation of seismic wave speeds

(Figure 7a) [Smith and Dahlen, 1973] without assuming a functional form of anisotropy. The opening angle  $d\theta$  is set to  $30^\circ$ , and we step from  $\theta = 0^\circ$  to  $\theta = 180^\circ - d\theta/2$  in  $d\theta/2$  increments. The  $r^0$ -related observables are collected as a function of  $\theta$ , providing direction-dependent wave speeds and hence anisotropy.

Rayleigh wave speeds derived from the angularly averaged  $\bar{A}(r, \tau = 0)$  distributions are denoted  $c$ . Since  $c = f\lambda$ , fast and slow wave speeds  $c^+$  and  $c^-$  are associated with propagation along the major and minor focal spot axis, respectively, and  $c^a$  denotes the anisotropy ratio  $c^+/c^-$ . We use the mean frequency for each band to obtain  $c$  from  $r^0$  or  $\lambda$  estimates. Considering the finite bandwidth, the dominant frequency may differ as a function of position, which can potentially introduce trends or artifacts in the resulting images. Each point on the grid is assigned three velocity estimates ( $c$ ,  $c^+$ , and  $c^-$ ), an anisotropy ratio ( $c^a$ ), and the angular average-based apparent attenuation coefficient ( $\alpha$ ; Figure 8). We do not evaluate azimuthally variable  $\alpha$  values.

## 6. Focal Spot Based Imaging Results

### 6.1. Low-Frequency Results (2 Hz)

We iterate that the images in Figures 8a–c and Figures 9a and 9b represent compilations of local estimates at the position of each pixel. No spatial smoothing is applied. At 2 Hz and 4 Hz, values are interpolated to a  $dx = 10$  m interval at  $x < 100$  m for the purpose of visualization. Figure 8a shows the results obtained from the low-frequency analysis. Azimuthal variability is well resolved due to the long seismic wavelength relative to the interstation distances (Figure 7a). Inferior results due to incomplete azimuthal averaging occurs along the edges and at the corners of the grid. We do not display the results along the edges. The  $\theta$ -average velocity estimates  $c$  (Figure 8a, left column) show fault-normal variations of about 25%, with an along-strike zone of reduced speeds between  $x = 300$  m and  $x = 500$  m. The smallest values are found in a 100 m wide and 200 m long zone between  $x = 400$  m and  $x = 500$  m, and  $y = 350$  m and  $y = 550$  m, to the NE of the fault. This zone corresponds to a local seismic trapping structure [Ben-Zion et al., 2015].

The smaller panels in the second column of Figure 8a show of the apparent attenuation ( $\alpha$ , top) and of the wave speeds in the fast direction ( $c^+$ , bottom). Variations within each image are also predominantly perpendicular to the fault strike. Compared to the  $c$  results the speed variation  $c^-$  along  $x$  is similarly smooth (not shown), whereas the  $c^+$  distribution (small bottom panels) shows a stronger variability with a zone of reduced fast velocities again between  $x = 300$  m and  $x = 500$  m. Stronger apparent attenuation is found in regions of low wave speed parallel to the fault at  $x > 300$  m. This general anticorrelation between relatively large  $\alpha$  and small  $c$ ,  $c^+$  values can also be found in details of the images. For example, the two small- $\alpha$  inclusions along  $x = 450$  m, at  $y = 100$  m and  $y = 300$  m, are compatible with the higher  $c$  values found at the same positions in the  $c^+$  and to a lesser degree in the  $c$  images.

The  $c^-$  (not shown) and  $c^+$  values are nowhere of similar size, which is illustrated by the anisotropy distribution  $c^a$  in the third column. The average anisotropy ratio is around 1.6, and regions of strongest anisotropy are found around  $x = 200$  m and  $y = 300$  m and along the NE edge of the grid between  $x = 500$  m and  $x = 600$  m.

The vector plots in Figure 7c show that the major axis is generally oriented parallel to the fault strike. Fast directions in the lower left portion of the area are gradually rotating toward the general fault-parallel trend. The grid search over  $\theta$  consistently returns the expected  $90^\circ$  angle between the major and minor axis (not shown); that is, the slow directions are mainly orthogonal to the fault strike.

All these results are meaningful since stable fits are obtained for essentially all directions (the few white “ $\theta$  completeness” in the corners of the  $c^+$  and  $c^a$  images outline the 0.75 fraction of the 13 tested directions that returned useful estimates). The spatial distributions of the RMS error  $\epsilon$  reveal an interesting zoning of the fit quality (Figure 9b) that provides complementary information about medium properties discussed in section 7.3.

### 6.2. Intermediate-Frequency Results (4 Hz)

The few white contours along the edges of the grid indicate that the seismic wavelengths at intermediate frequencies (Figure 7b) are sufficient to properly resolve most of the area. The obtained images (Figure 8b) reveal a larger medium heterogeneity with variations over smaller scales compared to the low-frequency results. The distributions of  $c$  (left column) now exhibit two along-strike zones of low velocities. The zone left of the fault along  $x = 200$  m is more continuous and characterized by smaller speeds compared to the more diffuse zone at  $x > 300$  m. The  $c^+$  distributions are also dominated by a fault-parallel zone of reduced velocities to the

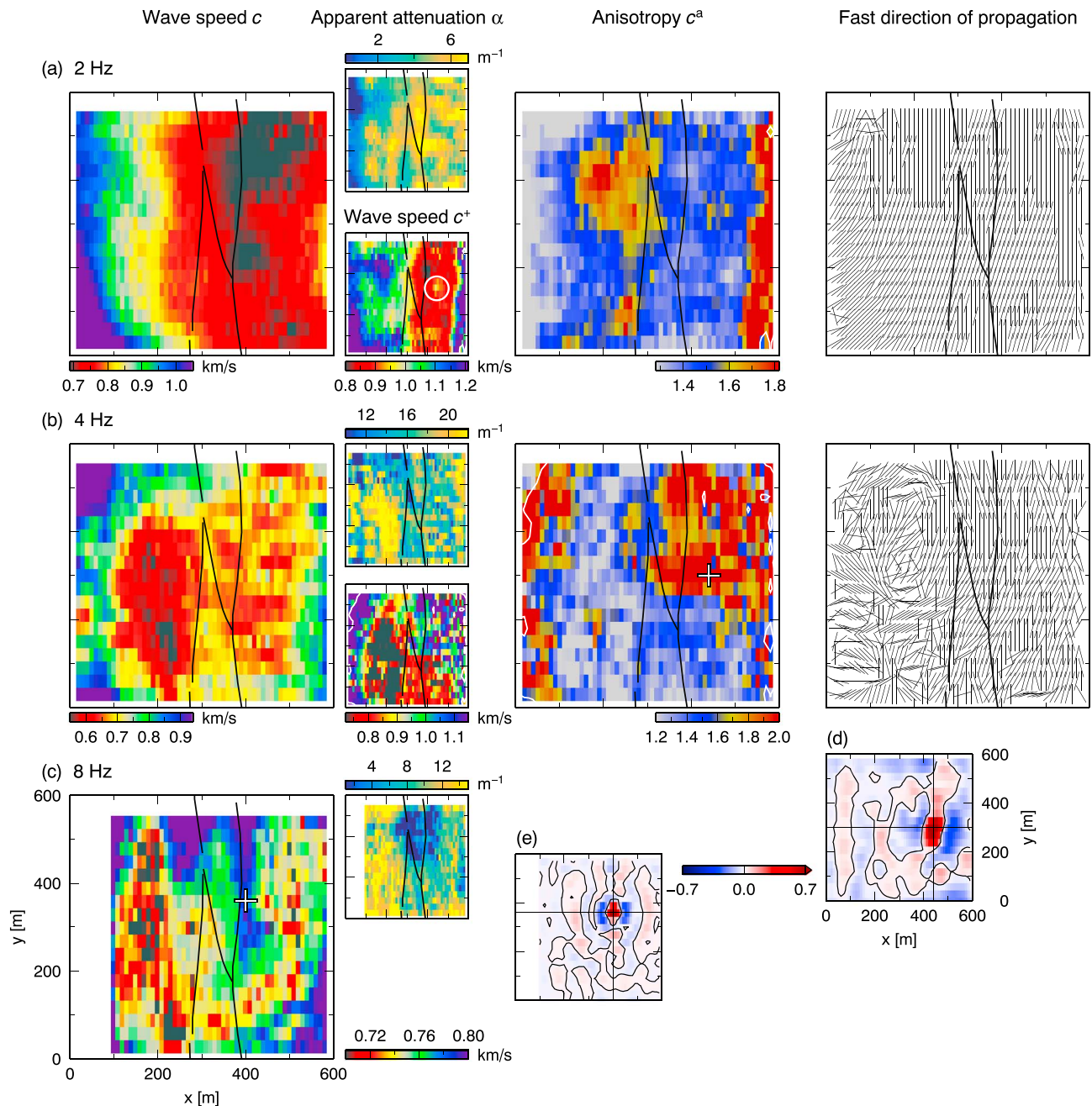


**Figure 8.** (a)–(c) Imaging results for the three frequencies. First column: Azimuthally averaged  $c$ . Second column; top: estimates of  $\alpha$ ; bottom:  $c^+$ . Third column: Anisotropy  $c^a$ . Fourth column: Directions of the major axis (fast propagation directions). (d)–(e) Selected scaled amplitude distributions and zero-level contours. White contours in (a), (b) trace the 0.75 ‘ $\theta$ -completeness.’ This refers to the line that separates areas in which the data fitting is stable in more/less than 75% of the tested directions. Fast directions are not indicated at locations inside the white contours. The white circle in the 2 Hz  $c^+$  image (a) highlights a scatterer. The cross in the 4 Hz  $c^a$  image (b) indicates the  $x_0, y_0$  position of the associated amplitude distribution in (d); it corresponds to Figure 5b, center column. The cross in the 8 Hz  $c$  image (c) indicates the  $x_0, y_0$  position of the associated amplitude distribution in (e); it corresponds to Figure 5b, right column. At 2 Hz and 4 Hz values are interpolated to a  $dx = 10$  m interval in the region  $x < 100$  m for the purpose of visualization. At 8 Hz the analysis is limited to  $x > 100$  m where  $dx = 10$  m.

left of the fault. Consistent with the low-frequency results, images of the  $\alpha$  coefficient show the same anti-correlated features as the  $c$  distributions. This supports the notion that  $\alpha$  represents physical attenuation to some degree.

Anisotropy is smallest in the lower left area exhibiting reduced velocities. It is largest in the top right quadrant ( $x, y > 300$  m) where extreme values around  $c^+/c^- = 3$  are obtained. These measurements may reflect

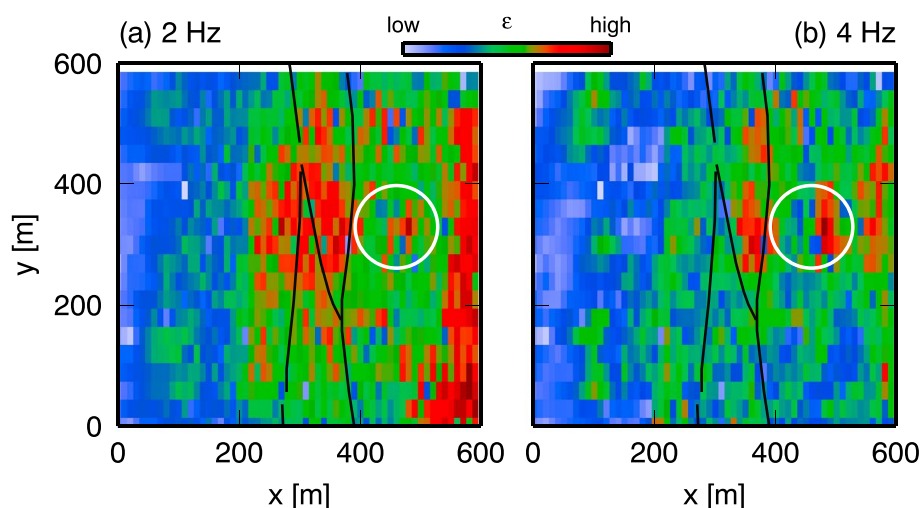


**Figure 9.** Spatial distributions of the RMS error estimate  $\epsilon$  obtained at (a) 2 Hz and (b) 4 Hz. The white circle indicates the high- $\epsilon$  values associated with a scatterer (see also Figure 8a).

true anisotropy of the damaged fault zone rocks. However, the results may also be potentially biased by the propagation regime inside the fault-parallel waveguide structure. The fault-parallel ripples in Figure 2 suggest that surface wave propagation in this region is by no means isotropic but resembles plane waves that propagate along the  $x$  direction. These signatures are compatible with fault zone reverberations [Hillers and Campillo, 2016], waves that are multiply reflected at the impedance contrasts. The zero contour line associated with reference stations in this region is not elliptical (Figure 8d) and indicates a poorly reconstructed focal spot. The elongation in the  $y$  direction with the missing nodal line controls the obtained very high  $c^+$  and hence anisotropy estimates. This also biases the average wave speed estimates in this area toward larger values. Additional data processing is required to mitigate the effects of such highly directional surface wave propagation.

The vector plots show the strike parallel alignment of the fast directions to the right of the fault. A vortex-like feature around  $x = 200$  m,  $y = 400$  m deviates from this general trend. This feature roughly delineates a local sedimentary basin hosting the infrastructure of the landowner.

### 6.3. High-Frequency Results (8 Hz)

Short seismic wavelengths allow a high-frequency analysis at  $x > 100$  m where  $dx = 10$  m (Figure 7c). Direction-dependent measurements cannot be obtained as too few points cover the focal spot shape in the  $y$  direction. The obtained  $c$  distribution (Figure 8c) is therefore less robust compared to the previous cases, as it is dominated by the behavior along the  $x$  direction where the station spacing is smallest. Yet the observations are useful because they extend the 4 Hz results. The 8 Hz  $c$  distribution also shows two zones of reduced velocities to the left and right of the mapped fault traces that are separated by a ridge of increased speeds. This green and blue ridge along the right fault trace overlaps partially with the trapping structure manifested by the low velocities in the 2 Hz and 4 Hz results in this area. However, the high-frequency focal spots are well recovered and do not show pathological elongations in the  $y$  direction (Figure 8e). The associated  $\alpha$  values confirm the trend observed in the previous frequency bands. Large values are found in the region at  $x < 250$  m that is also characterized by the smaller velocities. Smaller values correlate with the high-velocity ridge in the upper central portion of the panel. This anticorrelation is not met in the four corners and along the top and bottom edge, which—adopting the notion that  $\alpha$  has a physical meaning—points to insufficient sampling of the focal spot.

## 7. Discussion

The presented analysis and results demonstrate the utility of imaging local seismic characteristics in a challenging fault zone environment from properties of the focal spot. Clean surface wave spots can be obtained from zero lag cross-correlation amplitude fields that have been filtered in the wave number domain. In contrast to previous applications of reversed wavefield propagation in seismology, the focusing in the method

used here is reconstructed from data collected by a dense seismic array. Such dense arrays are similar to the high-resolution devices used in medical imaging [e.g., Catheline *et al.*, 2013], where the focal spot method facilitates clinical procedures.

### 7.1. Resolution

The resolution of the smallest and largest scales is governed by the interstation distance and the aperture of the array, respectively. Measurements can be made at all configurations where the distance  $r^0$  can be estimated from the  $A(r, \tau = 0)$  (or  $\bar{A}(r, \tau = 0)$ ) data. Considering 2 Hz data, we explored the differences between images compiled from grids that have constant  $dx = 30$  m, 20 m, and 10 m spacings. Together with the absence of regularization, this decrease in the  $dx$  spacing directly increases the resolution of velocity variations. The small interstation distance allows subwavelength resolution of sharp velocity contrasts [Catheline *et al.*, 2013] such as the high-velocity inclusion in the  $c^+$  image at  $x = 450$  m,  $y = 350$  m (white circle in Figure 8a). The larger misfit to the Bessel function model around this location that is also seen in the 4 Hz results (Figure 9) suggests that this feature is a scatterer [Hong *et al.*, 2005]. Recall the two different subwavelength scales here: sub- $\lambda$  resolution associated with the small interstation distance,  $dx, dy \ll \lambda$ ; and shape function fitting using data collected at sub- $\lambda$  distances from each reference location,  $r \leq 0.6\lambda$ .

The ease, elegance, and ability of the focal spot method to resolve simultaneously various properties of the shallow structure may be considered advantages over typical far-field tomographic imaging. The obtained distributions of elastic properties are compilations of point measurements that are estimated directly without smoothing the results in an inverse problem. The low-pass limit  $k_f$  in the wave number filter constitutes the only spatial averaging that we coupled to the spatial sampling. This filtering improves shape function fits, but it does not average over the estimated parameters at however closely spaced locations.

### 7.2. Relation of the Focal Spot Method to Other Diffuse Field Approaches

Assuming dominance of surface waves and homogeneous illumination, the properly scaled zero lag correlation field and the spatial autocorrelation coefficient (SPAC) [Aki, 1957] form a Fourier pair. We used this connection to derive the shape function equation (7) to parameterize the focal spot. The consistency between the time domain and spectral domain representations has been studied primarily for the 2-D case [Chávez-García and Luzón, 2005; Sánchez-Sesma and Campillo, 2006; Yokoi and Margaryan, 2008; Prieto *et al.*, 2009], but it has also been demonstrated in 1-D and 3-D [Nakahara, 2006]. Our analysis of the obtained fundamental mode Rayleigh wavefield could thus be considered a variation of the SPAC technique in the time domain. The spot size is evaluated using data at subwavelength distances because the complex fault zone velocity structure prohibits a consistent analysis at  $r > \lambda/2$ . Henstridge [1979] suggests the region around the first  $J_0(kr)$  zero crossing is also optimal for spectral domain estimates, although the analyzed  $kr$  range of observed SPAC spectra varies considerably between different studies [e.g., Smith *et al.*, 2013, and references therein].

Several differences exist between the focal spot method and SPAC implementations despite the formal Fourier pair relation. First, the importance of the wave number filter in our approach suggests that the SPAC method is not applicable in the present context because of the strong influence of fault zone waves and body waves on the zero lag correlation field and thus on the spatial autocorrelation coefficient. Second, the SPAC coefficient is defined as an azimuthal average, which implies that our approach is more advantageous because the focal spot can resolve anisotropy. Third, the design and limitations of mostly local arrays consisting of a limited number of stations is a matter of concern in the SPAC literature [e.g., Asten, 2006, and references therein]. Approaches having “features in common with SPAC” were also applied to USArray data at a continental scale [Ekström *et al.*, 2009]. In contrast, the data set analyzed here is obtained from a large USArray-like number of stations deployed in an area that is comparable to or somewhat larger than the footprint of a typical sparse SPAC array.

This dense array design leads us to discuss the zero lag fields using the concept of focal spot imaging. Both the reconstructed converging and diverging waves and the focal spot (Figure 2) suggest a time-reversal-based analysis of the spot size and shape in terms of the directional and wave-type-dependent diffraction limit. The time domain approach also facilitates the recorrelation of correlation coda ( $C^3$ ) for hypothesis testing. Finally, the refocusing perspective prepares for extensions targeting super resolution [e.g., Lerosey *et al.*, 2007].

The connection between diffuse wavefields and the Green's function implies that focal spots are also connected to the microtremor spectral ratio [Sánchez-Sesma *et al.*, 2011; García-Jerez *et al.*, 2013]. The local velocity

structure can potentially be estimated from ratios of horizontal and vertical component focal spots obtained from equipartitioned wavefields.

Focal spot based wave speed estimates have been shown to be consistent with far-field travel time inversions in elastography [Gallot *et al.*, 2011a] and seismology [Hillers *et al.*, 2014]. In the following section we compare our results to the noise-based Rayleigh group velocity distributions of Roux *et al.* [2016] based on the same data set.

### 7.3. Implications for the San Jacinto Fault Zone Environment

As mentioned, the overall features of our images are consistent with the basic structural results of Ben-Zion *et al.* [2015]. Considering the fast-varying velocity distributions with frequency and depth, and the different frequency bands used in the different studies, we do not expect to reproduce the images obtained by Roux *et al.* [2016] in all their detail. The velocity distributions show nevertheless a remarkable similarity in terms of the location and extension of the relevant features. This includes the prominent low-velocity zones around  $x = 400$  m obtained at 2 Hz and around  $x = 200$  m obtained at 4 Hz.

The important features in the  $c$ ,  $\alpha$ ,  $c^+$ ,  $c^a$ , and fast direction distributions cannot be attributed to topography (Figure 1b). Larger errors  $\epsilon$  at 2 Hz (Figure 9b) are generally found around and to the NE of the fault. Peak values along the right edge of the grid can be explained by the strong anisotropy  $c^a$  in this region (Figure 8a) which leads to larger spread around the azimuth-averaged  $J_0$  model (Figure 7). In contrast, the large  $\epsilon$  values between the mapped fault trace (Figure 9b) have no equivalent in the  $c^a$  maps. We attribute this deviation from the Bessel function model to scattering [Hong *et al.*, 2005]. The same general trend of stronger variations in the fault-normal direction is also observed in the 4 Hz results (Figure 9b).

The used frequency range is a proxy for depth considering that the local depth sensitivity of the Rayleigh wave focal spot is equal to the sensitivity of the overlapping far-field waves. Hillers *et al.* [2014] showed the resulting longitudinal polarization of the surface wave focal spot, which results from the vanishing of the vertical-radial component [Haney *et al.*, 2012]. The radial components of the backward- and forward-propagating Rayleigh waves cancel at time zero, leaving only the vertical component of motion. The associated eigenfunctions or depth-sensitivity kernels of the fundamental-mode Rayleigh waves are not affected by this interference.

Deeper parts imaged by longer wavelengths at 2 Hz are characterized by a fault-parallel low-velocity zone that has the shape of a wide U, with a minimum across a 200 m wide zone at  $x > 300$  m (Figure 8a). This is best expressed in the  $c^+$  distributions, that is, the fast wave speeds that are generally oriented parallel to the fault. Anisotropy is highest to the left and right of this channel. The 4 Hz and 8 Hz results exhibit smaller velocity variations at shallower depth. These distributions are characterized by two subparallel, discontinuous low-velocity zones, stronger apparent attenuation, stronger anisotropy, and spatially more complex fast directions. The region of reduced  $c$  velocities in the upper right is resolved at all frequencies, which is compatible with the waveguide character of this zone [Ben-Zion *et al.*, 2015]. The results suggest that this zone is continuous across the observed depth range which we roughly estimate to be the top 600 m to 800 m. In contrast, the fault-parallel low-velocity zone at  $x = 200$  m observed at high frequencies only is likely limited to shallow depth. The location and extent coincides with the local sedimentary basin to the left of the fault [Ben-Zion *et al.*, 2015]. Stations located inside this zone show elevated noise energy or amplified motion, similar to the depth-continuous trapping structure, but the shallow basin structure does not act as a waveguide.

The results at all frequencies show consistently a clear anticorrelation between wave speed and apparent attenuation, and a direct relation between wave speed and anisotropy. That is, the low-velocity regions are also characterized by stronger apparent attenuation and relatively low anisotropy, which is, however, still large compared to estimates observed in different environments. The overall consistency between our results and those obtained by Roux *et al.* [2016] implies that the focal spot velocity estimates are generally robust. A similar statement cannot yet be made for the patterns of apparent attenuation and anisotropy. The necessity of additional measurements highlights the usefulness of the focal spot method as it provides these important parameters in a single analysis.

The obtained anticorrelation between velocity and apparent attenuation is compatible with numerous field and laboratory observations of correlated velocity and  $Q$ . In particular, seismic trapping structures are associated with low velocities and strong attenuation [e.g., Ben-Zion *et al.*, 2003; Lewis *et al.*, 2005]. This reflects the larger seismic energy dissipation in less consolidated, softer, more damaged rocks characterized by reduced elastic moduli and seismic wave speeds. While we do not claim that the obtained nonzero  $\alpha$  estimates in the

$e^{-\alpha r}$  term— included for improved data fitting— represent an accurate proxy for  $Q$ , the consistent anticorrelation with velocity supports the notion that  $\alpha$  captures physical attenuation to some degree. Recall that the inference of attenuation properties in a reciprocal ( $h_{ij} = h_{ji}$ ) but dissipative medium is possible using reversed propagation even if the time-reversal symmetry is broken [Tanter et al., 2001; Fink, 2006].

The possibility of local anisotropy estimates is an important advantage of the focal spot method over traditional inversion methods. Anisotropy is a key observable that is caused by alignment of minerals, grains, or cracks under strain and hence linked to past [Ozacar and Zandt, 2009] or present [Boness and Zoback, 2006] stress states. It is therefore important for the understanding of the mechanics and dynamics of crustal deformation zones. Several studies using different data, techniques, and frequency ranges observe fast directions that are usually aligned with the system of strike-slip faults in the Southern California plate boundary region from the lower crust to the shallow depths imaged here [Lin et al., 2011; Rempe et al., 2013; Zigone et al., 2015; Li et al., 2015]. These independent results are compatible with the predominantly fault-parallel alignment of fast directions. Alignments away from this trend are mainly observed toward higher frequencies [Zigone et al., 2015]. The obtained vortex-like pattern to the left of the fault observed at 4 Hz is associated with a local sedimentary basin and highlights the resolution power of the focal spot method. Similar features emerge along the edges of subsidence areas [de Ridder et al., 2015]. The high degree of anisotropy obtained in this frequency range (Figure 8b) is also significantly larger compared to the sub-10% estimates reported by Lin et al. [2011], Zigone et al. [2015], and Li et al. [2015] at much longer periods.

The continuous low-velocity zone on the NE side of the mapped surface fault trace indicates rocks that are characterized by significantly reduced elastic moduli, which is typical for fault damage zones. The material is aligned in the direction of shear. In contrast, higher velocities to the SW of the fault obtained at lower frequencies indicate more competent material. Asymmetric damage patterns can result from repeated ruptures along faults between two different elastic bodies that are brought into contact by cumulative fault offset [Ben-Zion and Shi, 2005; Dor et al., 2006]. Regional tomographies [Tape et al., 2009; Allam and Ben-Zion, 2012; Zigone et al., 2015] indicate compositional contrasts across the San Jacinto fault that are compatible with the here obtained lower velocities to the NE of the Clark segment. Strong velocity variations are confined to the flower-shaped structures in the top few kilometers and are reduced by increasing normal stresses toward greater depths [Sylvester, 1988; Ben-Zion et al., 1992]. The focal spot method applied to data from a 600 m aperture array provides consistent high-resolution images of the top part of these mechanically susceptible faulting features. More generally, variation of damage with spatial scale can be investigated when velocity, anisotropy, and attenuation measurements are performed over a range of wavelengths. As demonstrated here, the focal spot method can be highly useful for integrated investigations of damage patterns in fault zone environments.

## 8. Conclusions

We imaged the complex shallow fault structure of the Clark branch of the San Jacinto fault zone based on properties of surface wave focal spots. “Local imaging in the absence of near-field waves” captures the essence of this method, which has long been used in acoustic time-reversal contexts and is applied here to seismological dense array data. Images of the obtained frequency-dependent seismic velocity distributions are consistent with structural features seen with noise amplitudes and small gunshots [Ben-Zion et al., 2015] as well as estimates of Rayleigh wave group velocities [Roux et al., 2016]. These consistencies support earlier agreement of far-field and focal spot imaging results [Gallot et al., 2011a; Hillers et al., 2014]. The accuracy of the simultaneously retrieved apparent attenuation and anisotropy distributions should be confirmed with independent measurements but are overall compatible with conclusions from other studies. The images show a prominent low-velocity waveguide structure to the NE of the fault that is continuous across the observed depth range and a second low-velocity structure to the SW associated with a shallow sedimentary basin. Strong apparent attenuation is generally observed in regions of low wave speeds. Directions of fast propagation are aligned parallel to the fault. Deviations from this trend imply greater structural complexity to the SW of the fault at shallower depths.

The wave number filtering for the removal of body wave and fault zone wave energy is required to obtain clean surface wave focal spots. Additional information gain may be marginal using inverse filter for the optimization of the focusing [Tanter et al., 2001] considering the generally robust focal spot reconstruction. However, strategies to mitigate the directionality effects inside the waveguide may well include inverse filtering [Gallot et al., 2011b] and normalizations applied in the wave number or eigenvector domain [Seydoux et al., 2015].

Extensions of the presented approach including reconstruction of nine-component correlation tensor spots, application of analytical expressions to describe their shape [Haney *et al.*, 2012] augmented by numerical experiments, and comparison to results obtained by other established methods are likely to support further the usefulness of the focal spot analysis as an efficient imaging tool in dense array seismology.

#### Acknowledgments

We thank A. Lecointre for computational assistance essential for this work and S. Catheline for discussions. The research was supported by the European Research Council (advanced grant WhisperL27507). G. Hillers acknowledges support through a Heisenberg fellowship from the German Research Foundation (HI 1714/1-2). Additional support was provided by the National Science Foundation (grant EAR-162061) and the Southern California Earthquake Center (based on NSF Cooperative agreement EAR-1033462 and USGS Cooperative agreement G12AC20038). Figures were made using GMT [Wessel and Smith, 1991]. The seismic data used in this study can be obtained from the Data Management Center of the Incorporated Research Institutions for Seismology. The paper benefitted from useful comments by M. Denolle, an anonymous referee, and Associate Editor G. Prieto.

#### References

- Abramowitz, M., and I. A. Stegun (1965), *Handbook of Mathematical Functions*, 1057 pp., Constable and Company, Dover ed., London.
- Aki, K. (1957), Space and time spectra of stationary stochastic waves, with special reference to microtremors, *Bull. Earthquake Res. Inst. Univ. Tokyo*, 35, 415–457.
- Aki, K., and P. G. Richards (1980), *Quantitative Seismology*, W. H. Freeman and Company, 1st ed., 932 pp., San Francisco, Calif.
- Allam, A. A., and Y. Ben-Zion (2012), Seismic velocity structures in the Southern California plate-boundary environment from double-difference tomography, *Geophys. J. Int.*, 190, 1181–1196, doi:10.1111/j.1365-246X.2012.05544.x.
- Asten, M. W. (2006), On bias and noise in passive seismic data from finite circular array data processed using SPAC methods, *Geophysics*, 71(6), V153–V162, doi:10.1190/1.2345054.
- Baysal, E., D. D. Kosloff, and J. W. C. Sherwood (1983), Reverse time migration, *Geophysics*, 48(11), 1514–1524.
- Ben-Zion, Y., and Z. Shi (2005), Dynamic rupture on a material interface with spontaneous generation of plastic strain in the bulk, *Earth Planet. Sci. Lett.*, 236, 486–496, doi:10.1016/j.epsl.2005.03.025.
- Ben-Zion, Y., S. Katz, and P. Leary (1992), Joint inversion of fault zone head waves and direct *P* arrivals for crustal structure near major faults, *J. Geophys. Res.*, 97, 1943–1951.
- Ben-Zion, Y., Z. Peng, D. Okaya, L. Seeber, J. G. Armbruster, N. Ozer, A. J. Michael, S. Baris, and M. Aktar (2003), A shallow fault-zone structure illuminated by trapped waves in the Karadere-Duzce branch of the North Anatolian Fault, western Turkey, *Geophys. J. Int.*, 152, 699–717.
- Ben-Zion, Y., et al. (2015), Basic data features and results from a spatially-dense seismic array on the San Jacinto fault zone, *Geophys. J. Int.*, 202, 370–380, doi:10.1093/gji/ggv14.
- Benech, N., S. Catheline, J. Brum, T. Gallot, and C. A. Negreira (2009), 1-D elasticity assessment in soft solids from shear wave correlation: The time-reversal approach, *IEEE Trans. Ultrason. Ferroelectr. Freq. Control*, 56(11), 2400–2410.
- Benech, N., J. Brum, S. Catheline, T. Gallot, and C. Negreira (2013), Near-field effects in Green's function retrieval from cross-correlation of elastic fields: Experimental study with application to elastography, *J. Acoust. Soc. Am.*, 133(5), 2755–2766, doi:10.1121/1.4795771.
- Boness, N. L., and M. D. Zoback (2006), A multiscale study of the mechanisms controlling shear velocity anisotropy in the San Andreas Fault Observatory at Depth, *Geophysics*, 71(5), F131–F146, doi:10.1190/1.2231107.
- Boué, P., P. Roux, M. Campillo, and X. Briand (2014), Phase velocity tomography of surface waves using ambient noise cross correlation and array processing, *J. Geophys. Res. Solid Earth*, 119, 519–529, doi:10.1002/2013JB010446.
- Capon, J. (1969), High-resolution frequency-wavenumber spectrum analysis, *Proc. IEEE*, 57(8), 1408–1418.
- Cassereau, D., and M. Fink (1992), Time-reversal of ultrasonic fields—Part III: Theory of the closed time-reversal cavity, *IEEE Trans. Ultrason. Ferroelectr. Freq. Control*, 39(5), 579–592.
- Catheline, S., N. Benech, J. Brum, and C. Negreira (2008), Time reversal of elastic waves in soft solids, *Phys. Rev. Lett.*, 100(6), 64301, doi:10.1103/PhysRevLett.100.064301.
- Catheline, S., R. Souchon, M. Rupin, J. Brum, and A. H. Dinh (2013), Tomography from diffuse waves: Passive shear wave imaging using low frame rate scanners, *Appl. Phys. Lett.*, 103, 14101, doi:10.1063/1.4812515.
- Chávez-García, F. J., and F. Luzón (2005), On the correlation of seismic microtremors, *J. Geophys. Res.*, 110, B11313, doi:10.1029/2005JB003671.
- Cox, H. (1973), Spatial correlation in arbitrary noise fields with application to ambient sea noise, *J. Acoust. Soc. Am.*, 54, 1289–1301, doi:10.1121/1.1914426.
- Cupillard, P., and Y. Capdeville (2010), On the amplitude of surface waves obtained by noise correlation and the capability to recover the attenuation: A numerical approach, *Geophys. J. Int.*, 181, 1687–1700, doi:10.1111/j.1365-246X.2010.04568.x.
- de Ridder, S. A. L., B. L. Biondi, and D. Nichols (2015), Elliptical-anisotropic eikonal phase velocity tomography, *Geophys. Res. Lett.*, 42, 758–764, doi:10.1002/2014GL062805.
- de Rosny, J., and M. Fink (2002), Overcoming the diffraction limit in wave physics using a time-reversal mirror and a novel acoustic sink, *Phys. Rev. Lett.*, 89(12), 124301, doi:10.1103/PhysRevLett.89.124301.
- Derode, A., A. Tourin, and M. Fink (2001), Random multiple scattering of ultrasound: II. Is time reversal a self-averaging process?, *Phys. Rev. E*, 64, 36606, doi:10.1103/PhysRevE.64.036606.
- Derode, A., E. Larose, M. Campillo, and M. Fink (2003), How to estimate the Green's function of a heterogeneous medium between two passive sensors? Application to acoustic waves, *Appl. Phys. Lett.*, 83(15), 3054–3056, doi:10.1063/1.1617373.
- Dor, O., T. K. Rockwell, and Y. Ben-Zion (2006), Geologic observations of damage asymmetry in the structure of the San Jacinto, San Andreas and Punchbowl faults in Southern California: A possible indicator for preferred rupture propagation direction, *Pure Appl. Geophys.*, 163, 301–349, doi:10.1007/s00024-005-0023-9.
- Ekström, G., G. A. Abers, and S. C. Webb (2009), Determination of surface-wave phase velocities across USArray from noise and Aki's spectral formulation, *Geophys. Res. Lett.*, 36, L18301, doi:10.1029/2009GL039131.
- Fink, M. (1997), Time reversed acoustics, *Physics Today*, 50(3), 34–40, doi:10.1063/1.881692.
- Fink, M. (1999), Time-reversed acoustics, *Sci. Am.*, 281, 91–97.
- Fink, M. (2006), Time-reversal acoustics in complex environments, *Geophysics*, 71(4), S1151–S1164, doi:10.1190/1.2215356.
- Fink, M., C. Prada, F. Wu, and D. Cassereau (1989), Self-focusing in inhomogeneous media with time-reversal acoustic mirrors, *Proc. IEEE Ultrason. Symp.*, 2, 681–686.
- Gallot, T., S. Catheline, P. Roux, J. Brum, N. Benech, and C. Negreira (2011a), Passive elastography: Shear-wave tomography from physiological-noise correlation in soft tissues, *IEEE Trans. Ultrason. Ferroelectr. Freq. Control*, 58(6), 1122–1126.
- Gallot, T., S. Catheline, P. Roux, and M. Campillo (2011b), A passive inverse filter for Green's function retrieval, *J. Acoust. Soc. Am.*, 131(1), EL21–EL27, doi:10.1121/1.3665397.
- García-Jerez, A., F. Luzón, F. J. Sánchez-Sesma, E. Lunedei, D. Albarello, M. A. Santoyo, and J. Almendros (2013), Diffuse elastic wavefield within a simple crustal model: Some consequences for low and high frequencies, *J. Geophys. Res. Solid Earth*, 118, 5577–5595, doi:10.1002/2013JB010107.
- Gerstoft, P., and T. Tanimoto (2007), A year of microseisms in Southern California, *Geophys. Res. Lett.*, 34, L20304, doi:10.1029/2007GL031091.
- Haney, M. M., and H. Nakahara (2014), Surface-wave Green's tensors in the near field, *Bull. Seismol. Soc. Am.*, 104(3), 1578–1586, doi:10.1785/0120130113.

- Haney, M. M., T. D. Mikesell, K. van Wijk, and H. Nakahara (2012), Extension of the Spatial Autocorrelation (SPAC) method to mixed-component correlations of surface waves, *Geophys. J. Int.*, *192*, 189–206, doi:10.1111/j.1365-246X.2012.05597.x.
- Hennino, R., N. Trégourès, N. M. Shapiro, L. Margerin, M. Campillo, B. A. van Tiggelen, and R. L. Weaver (2001), Observation of equipartitioning of seismic waves, *Phys. Rev. Lett.*, *86*(15), 3447–3450, doi:10.1103/PhysRevLett.86.3447.
- Henstridge, J. D. (1979), A signal processing method for circular arrays, *Geophysics*, *44*(2), 179–184.
- Hillers, G., and M. Campillo (2016), Fault zone reverberations from cross-correlations of earthquake waveforms and seismic noise, *Geophys. J. Int.*, *204*(3), 1503–1517, doi:10.1093/gji/ggv515.
- Hillers, G., M. Campillo, Y.-Y. Lin, K.-F. Ma, and P. Roux (2012), Anatomy of the high-frequency ambient seismic wave field at the TCDDP borehole, *J. Geophys. Res.*, *117*, B06301, doi:10.1029/2011JB008999.
- Hillers, G., Y. Ben-Zion, M. Landès, and M. Campillo (2013), Interaction of microseisms with crustal heterogeneity: A case study from the San Jacinto fault zone area, *Geochem. Geophys. Geosyst.*, *14*, 2182–2197, doi:10.1002/ggge.20140.
- Hillers, G., M. Campillo, Y. Ben-Zion, and P. Roux (2014), Seismic fault zone trapped noise, *J. Geophys. Res. Solid Earth*, *119*, 5786–5799, doi:10.1002/2014JB011217.
- Hillers, G., S. Husen, A. Obermann, T. Planès, E. Larose, and M. Campillo (2015), Noise-based monitoring and imaging of aseismic transient deformation induced by the 2006 Basel reservoir stimulation, *Geophysics*, *80*(4), 51–68, doi:10.1190/GEO2014-0455.1.
- Hong, T.-K., R.-S. Wu, and B. L. N. Kennett (2005), Stochastic features of scattering, *Phys. Earth Planet. Inter.*, *148*, 131–148, doi:10.1016/j.pepi.2004.08.002.
- Ishii, M., P. M. Shearer, H. Houston, and J. E. Vidale (2005), Extent, duration and speed of the 2004 Sumatra-Andaman earthquake imaged by the Hi-Net array, *Nature*, *435*, 933–936, doi:10.1038/nature03675.
- Larmat, C., J.-P. Montagner, M. Fink, Y. Capdeville, A. Tourin, and E. Clévédy (2006), Time-reversal imaging of seismic sources and application to the great Sumatra earthquake, *Geophys. Res. Lett.*, *33*, L19312, doi:10.1029/2006GL026336.
- Lerosey, G., J. de Rosny, A. Tourin, and M. Fink (2007), Focusing beyond the diffraction limit with far-field time reversal, *Science*, *315*, 1120–1122, doi:10.1126/science.1134824.
- Lewis, M. A., Z. Peng, Y. Ben-Zion, and F. L. Vernon (2005), Shallow seismic trapping structure in the San Jacinto fault zone near Anza, California, *Geophys. J. Int.*, *162*, 867–881, doi:10.1111/j.1365-246X.2005.02684.x.
- Li, Z., Z. Peng, Y. Ben-Zion, and F. L. Vernon (2015), Spatial variations of shear-wave anisotropy near the San Jacinto Fault Zone in Southern California, *J. Geophys. Res. Solid Earth*, *120*, 8334–8347, doi:10.1002/2015JB012483.
- Lin, F.-C., M. H. Ritzwoller, and R. Snieder (2009), Eikonal tomography: Surface wave tomography by phase front tracking across a regional broad-band seismic array, *Geophys. J. Int.*, *177*, 1091–1110, doi:10.1111/j.1365-246X.2009.04105.x.
- Lin, F.-C., M. H. Ritzwoller, Y. Yang, M. P. Moschetti, and M. J. Fouch (2011), Complex and variable crustal and uppermost mantle seismic anisotropy in the western United States, *Nat. Geosci.*, *4*, 55–61, doi:10.1038/ngeo1036.
- Lin, F.-C., D. Li, R. W. Clayton, and D. Hollis (2013), High-resolution 3D shallow crustal structure in Long Beach, California: Application of ambient noise tomography on a dense seismic array, *Geophysics*, *78*(4), Q45–Q56, doi:10.1190/GEO2012-0453.1.
- Liu, X., and Y. Ben-Zion (2013), Theoretical and numerical results on effects of attenuation on correlation functions of ambient seismic noise, *Geophys. J. Int.*, *194*, 1966–1983, doi:10.1093/gji/ggt215.
- McMechan, G. A. (1982), Determination of source parameters by wavefield extrapolation, *Geophys. J. R. Astron. Soc.*, *71*, 613–628.
- Mordret, A., N. M. Shapiro, S. S. Singh, P. Roux, and O. I. Barkedv (2013), Helmholtz tomography of ambient noise surface wave data to estimate Scholte wave phase velocity at Valhall Life of the Field, *Geophysics*, *78*(2), WA99–WA109, doi:10.1190/GEO2012-0303.1.
- Nakahara, H. (2006), A systematic study of theoretical relations between spatial correlation and Green's function in one-, two- and three-dimensional random scalar wavefields, *Geophys. J. Int.*, *167*, 1097–1105, doi:10.1111/j.1365-246X.2006.03170.x.
- Nakata, N., J. P. Chang, J. F. Lawrence, and P. Boué (2015), Body wave extraction and tomography at Long Beach, California, with ambient-noise interferometry, *J. Geophys. Res. Solid Earth*, *120*, 1159–1173, doi:10.1002/2015JB011870.
- Olivier, G., F. Brenguier, M. Campillo, R. Lynch, and P. Roux (2015), Body-wave reconstruction from ambient seismic noise correlations in an underground mine, *Geophysics*, *80*(3), KS11–KS25, doi:10.1190/geo2014-0299.1.
- Ozacar, A. A., and G. Zandt (2009), Crustal structure and seismic anisotropy near the San Andreas Fault at Parkfield, California, *Geophys. J. Int.*, *178*, 1098–1104, doi:10.1111/j.1365-246X.2009.04198.x.
- Prieto, G. A., J. F. Lawrence, and G. C. Beroza (2009), Anelastic Earth structure from the coherency of the ambient seismic field, *J. Geophys. Res.*, *114*, B07303, doi:10.1029/2008JB006067.
- Prieto, G. A., M. Denolle, J. F. Lawrence, and G. C. Beroza (2011), On amplitude information carried by the ambient seismic field, *C. R. Geosci.*, *343*, 600–614, doi:10.1016/j.crte.2011.03.001.
- Rempe, M., T. Mitchell, J. Renner, S. Nippres, Y. Ben-Zion, and T. Rockwell (2013), Damage and seismic velocity structure of pulverized rocks near the San Andreas Fault, *J. Geophys. Res. Solid Earth*, *118*, 2813–2831, doi:10.1002/jgrb.50184.
- Rietbrock, A., and F. Scherbaum (1994), Acoustic imaging of earthquake sources from the Chalfant Valley, 1986, aftershock series, *Geophys. J. Int.*, *119*, 260–268.
- Rost, S., and C. Thomas (2002), Array seismology: Methods and applications, *Rev. Geophys.*, *40*(3), 1008, doi:10.1029/2000RG000100.
- Roux, P., L. Moreau, A. Lecointre, G. Hillers, M. Campillo, Y. Ben-Zion, D. Zigone, and F. Vernon (2016), A methodological approach towards high-resolution seismic imaging of the San Jacinto Fault Zone using ambient-noise recordings at a spatially dense array, *Geophys. J. Int.*, *206*, 980–992, doi:10.1093/gji/ggw193.
- Sabra, K. G., P. Gerstoft, P. Roux, W. A. Kuperman, and M. C. Fehler (2005), Surface wave tomography from microseisms in Southern California, *Geophys. Res. Lett.*, *32*, L14311, doi:10.1029/2005GL023155.
- Sánchez-Sesma, F. J., and M. Campillo (2006), Retrieval of the Green's function from cross correlation: The canonical elastic problem, *Bull. Seismol. Soc. Am.*, *96*(3), 1182–1191, doi:10.1785/0120050181.
- Sánchez-Sesma, F. J., et al. (2011), A theory for microtremor  $H/V$  spectral ratio: Application for a layered medium, *Geophys. J. Int.*, *186*, 221–225, doi:10.1111/j.1365-246X.2011.05064.x.
- Schulte-Pelkum, V., P. S. Earle, and F. L. Vernon (2004), Strong directivity of ocean-generated seismic noise, *Geochem. Geophys. Geosyst.*, *5*, Q03004, doi:10.1029/2003GC000520.
- Seydoux, L., N. Shapiro, J. de Rosny, and M. Landès (2015), A spatial coherence analysis of seismic wavefields based on array covariance matrix: Application to one year of USArray data, Abstract S34B-04 presented at 2015 Fall, AGU, San Francisco, Calif., 14–18 Dec.
- Shapiro, N. M., M. Campillo, L. Stehly, and M. H. Ritzwoller (2005), High-resolution surface-wave tomography from ambient seismic noise, *Science*, *307*, 1615–1618, doi:10.1126/science.1108339.
- Smith, M. L., and F. A. Dahlen (1973), The azimuthal dependence of Love and Rayleigh wave propagation in a slightly anisotropic medium, *J. Geophys. Res.*, *78*(17), 3321–3333.

- Smith, N. R. A., A. M. Reading, M. W. Asten, and C. W. Funk (2013), Constraining depth to basement for mineral exploration using microtremor: A demonstration study from remote inland Australia, *Geophysics*, *78*(5), B227–B242, doi:10.1190/GEO2012-0449.1.
- Smith, S. W. (1997), *The Scientist and Engineer's Guide to Digital Signal Processing*, 626 pp., California Technical Publ., San Diego, Calif.
- Spudich, P., and D. Oppenheimer (1986), Dense seismograph array observations of earthquake rupture dynamics, in *Earthquake Source Mechanics*, *Geophys. Monogr.*, vol. 37, edited by P. Spudich and D. Oppenheimer, pp. 285–296, AGU, Washington, D. C.
- Stehly, L., M. Campillo, B. Froment, and R. L. Weaver (2008), Reconstructing Green's function by correlation of the coda of the correlation ( $C^3$ ) of ambient seismic noise, *J. Geophys. Res.*, *113*, B11306, doi:10.1029/2008JB005693.
- Sylvester, A. G. (1988), Strike-slip faults, *Geol. Soc. Am. Bull.*, *100*, 1666–1703.
- Tanter, M., J.-L. Thomas, and M. Fink (2000), Time reversal and the inverse filter, *J. Acoust. Soc. Am.*, *108*(1), 223–234.
- Tanter, M., J.-F. Aubry, J. Gerber, J.-L. Thomas, and M. Fink (2001), Optimal focusing by spatio-temporal inverse filter: I. Basic principles, *J. Acoust. Soc. Am.*, *110*(1), 37–47, doi:10.1121/1.1377051.
- Tape, C., Q. Liu, A. Maggi, and J. Tromp (2009), Adjoint tomography of the Southern California crust, *Science*, *325*, 988–992, doi:10.1126/science.1175298.
- Tromp, J., C. Tape, and Q. Liu (2005), Seismic tomography, adjoint methods, time reversal and banana-doughnut kernels, *Geophys. J. Int.*, *160*, 195–216, doi:10.1111/j.1365-246X.2004.02453.x.
- Tsai, V. C. (2010), An explicit relationship between time-domain noise correlation and spatial autocorrelation (SPAC) results, *Geophys. J. Int.*, *182*, 454–460, doi:10.1111/j.1365-246X.2010.04633.x.
- Tsai, V. C. (2011), Understanding the amplitudes of noise correlation measurements, *J. Geophys. Res.*, *116*, B09311, doi:10.1029/2011JB008483.
- Walker, K. T., and P. M. Shearer (2009), Illuminating the near-sonic rupture velocities of the intracontinental Kokoxili  $M_w$  7.8 and Denali fault  $M_w$  7.9 strike-slip earthquakes with global  $P$  wave back projection imaging, *J. Geophys. Res.*, *114*, B02304, doi:10.1029/2008JB005738.
- Wessel, P., and W. H. F. Smith (1991), Free software helps map and display data, *Eos Trans. AGU*, *72*, 445–446.
- Yokoi, T., and S. Margaryan (2008), Consistency of the spatial autocorrelation method with seismic interferometry and its consequence, *Geophys. Prospect.*, *56*, 435–451, doi:10.1111/j.1365-2478.2008.00709.x.
- Zigone, D., Y. Ben-Zion, M. Campillo, and P. Roux (2015), Seismic tomography of the Southern California plate boundary region from noise-based Rayleigh and Love waves, *Pure Appl. Geophys.*, *172*, 1007–1032, doi:10.1007/s00024-014-0872-1.